MASTERARBEIT | MASTER'S THESIS

Titel | Title

Function and Localization of ParA ATPase like MinD in Methanogenic Archaea

verfasst von | submitted by

Sharanya Sridhara

angestrebter akademischer Grad | in partial fulfilment of the requirements for the degree of

Master of Science (MSc)

Wien | Vienna, 2026

Studienkennzahl lt. Studienblatt | Degree programme code as it appears on the student record sheet:	UA 066 865
Studienrichtung lt. Studienblatt | Degree programme as it appears on the student record sheet:	Masterstudium Molecular Biology
Betreut von | Supervisor:	Mag. Mag. Dr.techn. Simon Karl-Maria Rasso Rittmann Privatdoz. Bakk.
Mitbetreut von | Co-Supervisor:	Mag. Nika Pende MSc PhD

Contents

Acknowledgements

I would first like to express my sincere gratitude to my supervisor, Dr. Simon K.-M. R. Rittmann, Privatdoz., for giving me the opportunity to carry out my master's thesis in his laboratory. I am thankful for his guidance, patience, and constructive feedback, as well as for the time he invested in carefully reviewing my thesis and providing valuable scientific input.

I am especially grateful to my co-supervisor, Dr. Nika Pende, for her continuous support throughout my master's thesis journey. Her guidance, encouragement and availability at every stage of the project were invaluable. She consistently provided clear direction, thoughtful advice and unwavering support, which greatly contributed to my scientific development and confidence as a researcher. I sincerely thank her for her kindness, generosity and mentorship, which played a crucial role in shaping both my project and my personal growth.

I would also like to thank Assoc. Prof. Dr. Silvia Bulgheresi for her continuous support and insightful guidance during the Environmental Cell Biology laboratory group meetings. Her valuable suggestions and critical discussions helped keep my project on track and significantly contributed to its smooth progress.

I am very grateful to Dr. Tobias Viehboeck for his important contributions to my project, particularly for providing insights into experimental protocols and for performing the required bioinformatics and in vivo analyses. I would like to thank Nicole Krause, M.Sc., who, despite her PhD commitments, always offered a helping hand in the laboratory and provided consistent support whenever needed. I am also thankful to Arnau Sabater i Mezquita, M.Sc., for his patience and readiness to help in the lab, always taking the time to explain procedures clearly and thoroughly. I additionally thank all fellow master's students for their constant support and collaborative spirit throughout my project.

Lastly, I would like to thank Ulf Naumann, as well as all technicians and laboratory assistants, for maintaining a supportive and well-organized laboratory environment that ensured the smooth running of experiments. I am also deeply thankful to the entire Archaea Biology and Ecogenomics Department, including the PhD students and postdoctoral researchers, for creating a welcoming, positive, and encouraging atmosphere in the lab and beyond. The kindness, support and collegiality of everyone in the department played an important role in enabling me to successfully complete my work.

Abstract

Archaeal cell division displays remarkable diversity, combining bacterial and eukaryotic like mechanisms. Many euryarchaeal lineages divide using the tubulin homolog FtsZ and also encode MinD. MinD is a deviant Walker-type ATPase related to the bacterial Min system and the ParA superfamily. In bacteria, the MinCDE system is negatively regulating FtsZ, thereby allowing for its placement at mid cell during division. However, the function of archaeal MinD remains poorly understood.

In this study, the role of MinD was investigated in two methanogenic archaea, *Methanobrevibacter smithii* and *Methanopyrus kandleri*, both of which encode FtsZ-based division systems and multiple MinD homologs. We tested whether archaeal MinD functions in FtsZ positioning, as in bacteria, or instead acts as a ParA-like ATPase involved in chromosome associated processes.

Biochemical assays demonstrated that MinD from both organisms is an active ATPase. Immunolabelling and quantitative image analysis showed that MinD does not function as a negative regulator of FtsZ placement. Instead, MinD displayed spatial associations with the nucleoid during cell-cycle progression. In silico prediction and electrophoretic mobility shift assays indicated DNA-binding capacity and co-immunoprecipitation identified interaction partners enriched for DNA and RNA associated proteins.

Together, these results support a model in which MinD in methanogenic archaea is functionally distinct from bacterial MinD and is more closely associated with chromosome biology than with division site positioning.

As a separate part of my thesis, the role of SepF in *M. kandleri* was investigated. In archaea SepF is the anchor of FtsZ division ring. Immunolabelling and quantitative image analysis showed that SepF co-localizes with FtsZ in *M. kandleri*, pointing to its role in FtsZ-anchoring.

Zusammenfassung

Die Zellteilung bei Archaeen ist bemerkenswert vielfältig und kombiniert bakterielle und eukaryotische Mechanismen. Viele Euryarchaeota verwenden das Tubulin-Homolog FtsZ um sich zu teilen, und außerdem kodieren sie MinD. MinD ist eine Walker-Typ-ATPase, die mit dem bakteriellen Min-System und der ParA-Superfamilie phylogenetisch verwandt ist. In Bakterien reguliert das MinCDE-System FtsZ negativ und ermöglicht so seine Polymerisierung in der Zellmitte während der Teilung. Die Funktion von MinD wurde in Archaea noch nicht aufgeklärt.

In dieser Studie wurde die Rolle von MinD in zwei methanogenen Archaeen, *Methanobrevibacter smithii* und *Methanopyrus kandleri*, untersucht. Beide haben ein auf FtsZ-basierendes Teilungssysteme und kodieren mehrere MinD-Homologe. Ziel war es zu testen, ob archaeales MinD wie in Bakterien bei der Positionierung von FtsZ fungiert oder stattdessen als ParA-ähnliche ATPase wirkt, die an chromosomassoziierten Prozessen beteiligt ist.

Biochemische Assays zeigten, dass MinD aus beiden Organismen eine aktive ATPase ist. Immunmarkierung und quantitative Bildanalyse zeigten, dass MinD nicht als negativer Regulator von FtsZ fungiert. Stattdessen zeigte MinD während des Zellzyklusverlaufs räumliche Assoziation mit dem Nukleoid. In-silico-Analysen und elektrophoretische Mobilitätsverschiebungsassays deuteten auf die Fähigkeit hin DNA zu binden, und Co-Immunpräzipitation identifizierte Interaktionspartner, die angereichert an DNA- und RNA-assoziierten Proteinen waren.

Zusammen stützen diese Ergebnisse ein Modell, in dem sich MinD in methanogenen Archaeen funktionell von bakteriellem MinD unterscheidet und enger mit der Chromosomenbiologie als mit der Positionierung der Teilungsebene verbunden ist.

Als separater Teil meiner Masterarbeit wurde die Rolle von SepF in *M. kandleri* untersucht. In Archaea ist SepF der Anker des FtsZ-Rings. Immunmarkierung und quantitative Bildanalyse zeigten, dass SepF in *M. kandleri* mit FtsZ co-lokalisiert, was auf seine Rolle bei der FtsZ-Ankerung hinweist.

Introduction

Cell division is one of the most fundamental and ancient biological processes for the continuity of life. It ensures the transmission of genetic material from the mother cell to daughter cells and is tightly coordinated with other essential cellular events such as DNA replication and segregation, membrane and envelope biosynthesis, cytokinesis and ultimately abscission - the physical separation of daughter cells (Bernander, R., & Ettema, T. J. G., 2010; Adams & Errington, 2009). In all domains of life, these events must be precisely regulated in time and space to maintain genome stability, cell shape and viability.

While the overarching goal of cell division is conserved, the molecular machineries that accomplish this process have diversified considerably across Bacteria, Archaea and Eukarya, reflecting their distinct evolutionary trajectories and cellular architectures (Eme et al., 2017; Makarova et al., 2010). Among these, Archaea occupy a particularly fascinating evolutionary position, sharing certain structural and informational features with eukaryotes while resembling bacteria in cell organization and ecological distribution.

Archaea exhibit an extraordinary diversity of cell shapes and sizes, rivalling that of bacteria. Many archaeal species are coccoid or rod-shaped, but others form unusual morphologies, including flat squares, triangles and filamentous or irregular forms, revealing a striking degree of morphological plasticity (van Wolferen et al., 2022). For example, species of *Haloquadratum walsbyi* grow as perfectly flat square cells that assemble into sheets, whereas *Methanospirillum hungatei* forms long filamentous chains enclosed within a proteinaceous sheath (Kandler & König, 1998; Albers & Meyer, 2011). This morphological diversity is mirrored by the variety of cytoskeletal and envelope systems used to shape and divide the archaeal cell.

The Archaeal Cell Envelope

Unlike most bacteria, which typically possess a peptidoglycan (PG) cell wall, the majority of archaea lack PG and instead rely on a surface-layer (S-layer) as the main structural and protective component of their cell envelope (Albers & Meyer, 2011; Meyer & Albers, 2020). The S-layer is a two-dimensional crystalline lattice composed of protein or glycoprotein subunits that form repetitive arrays with defined symmetries - oblique (p2), square (p4), or hexagonal (p3 or p6) — depending on the species and lattice geometry (Albers & Meyer, 2011).

The structural organization of archaeal S-layers varies between lineages but is typically composed of two major glycoproteins**:** SlaA, forming the outer lattice, and SlaB, anchoring the lattice to the cytoplasmic membrane (Baumeister, W., & Lembcke, G. (1992); Meyer & Albers, 2020). In the crenarchaeon *Sulfolobus solfataricus*, silencing of the *slaB* gene leads to profound defects in cell envelope integrity: the S-layer becomes disorganized, glycosylation patterns are altered and cells display aberrant morphologies and failed division events (Zink et al., 2019). This demonstrates that the S-layer is not merely a passive coat but an essential structural determinant that integrates cell-shape maintenance, envelope biogenesis and cytokinesis.

Interestingly, not all archaea rely on an S-layer as their primary cell-envelope structure. Most representatives of the Methanobacteriales and Methanopyrales lack an S-layer and instead possess a PG cell wall, that superficially resembles bacterial PG, but is chemically and biosynthetically distinct. Archaeal PG (Mukhopadhyay, 2024) is composed of N-acetylglucosamine (NAG) and N-acetyltalosaminuronic acid (NAT) linked by β(1→3) glycosidic bonds and its peptide crosslinks use L-amino acids rather than D-amino acids, making it resistant to lysozyme and most β-lactam antibiotics (Albers & Meyer, 2011; König et al., 2017).

Members of the Methanobacteriales and Methanopyrales are the only known archaeal lineages to harbor this rigid PG layer. Remarkably, these groups are also the only archaea to encode homologs of the bacterial actin-like protein MreB (Makarova et al., 2010), which in bacteria is contributing to cell shape maintenance and coordinating PG synthesis (Errington, 2015).

Archaeal Cell Division: Evolutionary Context and Mechanistic Diversity

Although the overall objective (faithful transmission of genetic material and equitable partitioning of cytoplasm) is shared across life, the molecular machines that execute cytokinesis differ markedly between the domains and have been repurposed and combined in many lineages. In eukaryotes, membrane scission during abscission is largely accomplished by the endosomal sorting complex required for transport (ESCRT) machinery, in particular ESCRT-III polymers and the AAA+ ATPase VPS4, which assemble at the midbody to mediate membrane neck constriction and severing (reviewed in Vietri et al., 2020). In bacteria, cytokinesis is organised around the tubulin homolog FtsZ, which polymerizes into a dynamic Z-ring at midcell and recruits the divisome — a multi-protein complex that synthesizes and remodels PG while constricting the membrane. Z-ring placement is controlled by negative

regulators such as the Min system and nucleoid occlusion systems to ensure mid-cell assembly (Thanbichler, 2010; McQuillen & Xiao, 2021). Archaea occupy an intermediate and highly diverse position: depending on the archaeal group, either FtsZ-based systems, ESCRT-III/Vps4-like systems, actin-like cytoskeletal elements (e.g., Crenactin), or combinations thereof are used for cell division. The particular choice of machinery correlates with phylogeny and envelope architecture (Ithurbide, Albers, Gribaldo & Pende, 2022). This diversity highlights that prokaryotic cytokinesis has been reshaped many times through evolution, yielding a mosaic of FtsZ, ESCRT and actin/tubulin usages across archaeal lineages.

FtsZ-based Cell Division

FtsZ is a GTP-binding tubulin homolog that forms protofilaments capable of curvature and dynamic treadmilling; these properties allow FtsZ to act both as a scaffold and as a generator of constrictive forces (Aylett & Duggin, 2017; Wagstaff & Löwe, 2018). FtsZ is conserved between bacteria and archaea (Euryarchaeota, DPANN and more patchy in other linages), however, archaeal lack most other divisome components with the exception of SepF, MinD, and in the case of Methanopyrales FtsA (Ithurbide et al., 2022) (Fig.1). In many archaea that deploy FtsZ, the system shows lineage-specific elaborations. A recurring pattern in several euryarchaeal and DPANN species is the presence of two FtsZ paralogues (commonly named FtsZ1 and FtsZ2). Studies in the halophilic euryarchaeon *Haloferax volcanii* show that FtsZ1 and FtsZ2 generally co-localize at midcell over the cell cycle yet have separable functions: FtsZ1 contributes predominantly to ring assembly and acts as a spatial organizer, whereas FtsZ2 is more directly implicated in the constriction step (Liao & Ithurbide et al., 2021). Importantly, genetic and imaging work indicates interdependence between the two paralogues: FtsZ2 assembly and stability depend on FtsZ1, and FtsZ1 ring condensation receives positive feedback from correctly functioning FtsZ2, a relationship that implies a coordinated two-component division system where one paralogue templates or regulates the other (Liao & Ithurbide et al., 2021).

Anchoring and regulation of archaeal FtsZ rings also differ from bacterial paradigms. SepF, a small dimeric protein that cooccurs with FtsZ in archaea, colocalizes with FtsZ at midcell and serves as a membrane anchor and modulator of filament architecture (Pende & Sogues et al., 2021). In *H. volcanii*, SepF co-localizes with both FtsZ1 and FtsZ2 at the division plane and is essential for normal cell division. Biochemical assays and interaction studies indicate that SepF interacts preferentially with FtsZ2 while its midcell localization nonetheless depends on the

FtsZ1 network, pointing to hierarchical coordination between the two FtsZ paralogues and their anchors (Nußbaum et al., 2021). Recent work has further identified archaeal division accessory proteins termed CdpB1 and CdpB2 that co-localize with SepF at midcell. The absence of these factors disrupts organization of the FtsZ/SepF ring and leads to division defects, while biochemical mapping indicates that SepF binds CdpB1 (but not CdpB2) and that CdpB1 and CdpB2 form a complex with SepF, suggesting a trimeric stabilizing assembly at the cytokinetic site (Nußbaum et al., 2023). Contrary to *H. volcanii*, the methanogenic archaeaon *Methanobrevibacter smithii* uses a single FtsZ homolog (FtsZ1) for its cell division rather than the two FtsZ-based (FtsZ1/FtsZ2) system found in most other Euryarchaea. The structural, cellular and biochemical study by Pende & Sogues *et al.* (2021) established that SepF is the archaeal membrane anchor for FtsZ in *M. smithii*, and likely in all other FtsZ-containig archaea based on phylogenomic analysis. The SepF of *M. smithii* was found to bind and deform liposomes, pointing to its membrane-binding function. Further, crystal structure and interaction assays showed that the functional SepF dimer is interacting with the C-terminal domain of FtsZ and SepF is bundling FtsZ filaments. Membrane binding and FtsZ filament bundling are both features conserved between bacteria and archaea, even if the dimerization interface of the SepF dimer differs between bacteria and archaea. In *M. smithii* cells, FtsZ and SepF co-localize at the septation plane and SepF marks the future division sites within prospective daughter cells, suggesting a degree of division-site pre-patterning or priming mediated by SepF, something unique to *M. smithii* (Pende & Sogues et al., 2021).

The findings from these two model-archaea illustrate that the so far identified archaeal divisomes components are functionally modular and incorporate lineage-specific adaptors that tune how the Z-ring engages in cell division.

Complementing the FtsZ/SepF system, some archaeal species employ other cytoskeletal systems for shape and division control (Fig. 1). CetZ1, a tubulin-like protein in *H. volcanii*, is required for differentiation into a rod-shaped morphology and is essential for normal swimming motility. CetZ1 assembles into dynamic cytoskeletal structures that remodel the envelope and direct rod formation, suggesting a division of labour in which FtsZ manages cytokinesis while CetZ proteins tune cell shape and envelope remodelling needed for certain life-styles (Duggin et al., 2015). Within the TACK superphylum, actin-like proteins such as Crenactin in *Pyrobaculum calidifontis* form double-helical filaments controlled by Arcadin factors and are associated with rod-shaped morphology and possibly cytokinesis, highlighting that actin-

family polymers also participate in archaeal cell biology beyond the classical FtsZ/ESCRT dichotomy (Ettema et al., 2011; Izoré et al., 2016).

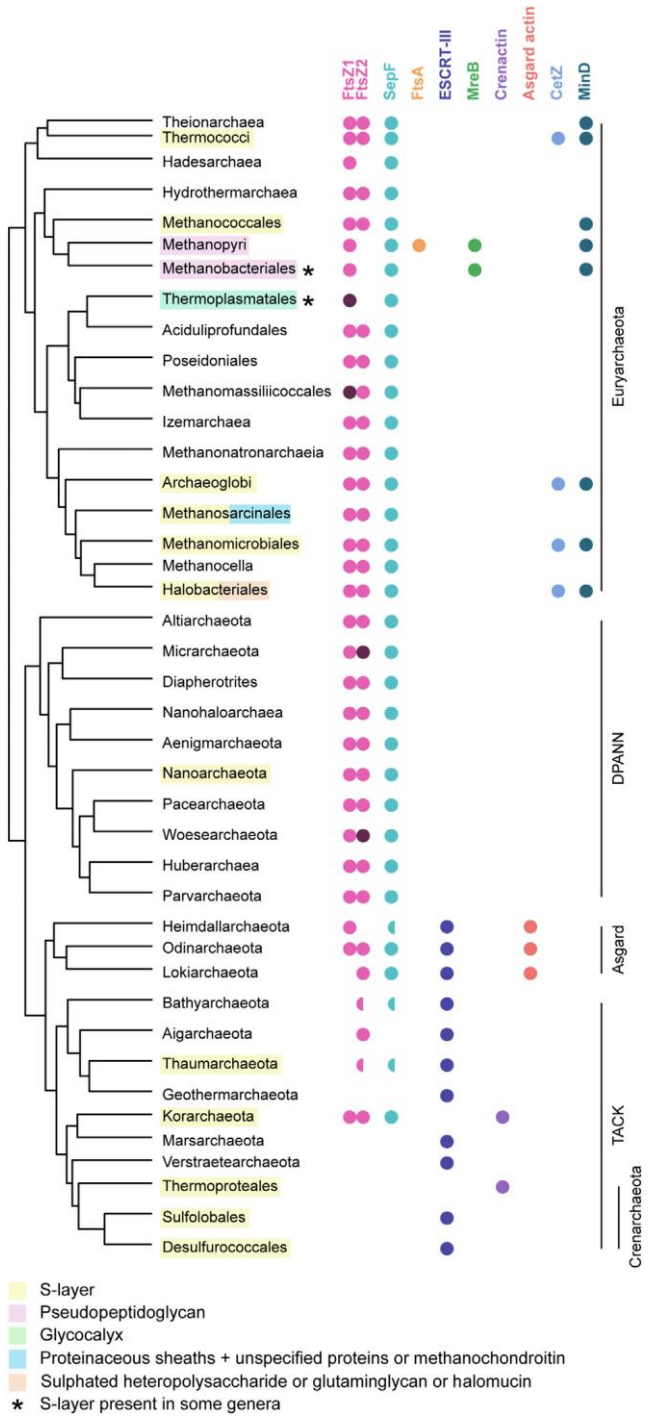

Figure 1: Archaeal cell envelope types and distribution of genes involved in archaeal cell division and spatial organization. Distribution of FtsZ1 and FtsZ2 (magenta, dark magenta if more copies are present), SepF (turquoise), FtsA (orange), ESCRT-III (CdvB and homologs; dark purple), MreB (green), Crenactin (light purple), Asgard actin (salmon), CetZ (violet), and MinD (teal) homologs on a schematic reference phylogeny of the archaea together with indication of cell envelope types. Semicircles: corresponding protein could not be identified in all the taxa. Figure taken from Ithubide et al. 2022.

Archaeal MinD

Notably, not all archaeal FtsZ systems conform to the bacterial MinCDE-driven spatial logic. In bacteria, MinD is a membrane-associated ATPase that recruits MinC to prevent aberrant Z-ring formation near the poles, and its ATPase activity and release from the membrane is

stimulated by MinE (Vecchiarelli et al., 2014). However, archaeal genomes lack MinC and MinE homologs, suggesting that archaeal MinD has diverged functionally (Nußbaum et al., 2020). In *H. volcanii*, four MinD homologues are encoded in the genome, yet deletion studies showed that loss of MinD paralogues does not perturb Z-ring placement, cell size or the ability to septate (Nußbaum et al., 2020) (Fig.2). Rather than serving as a division-site oscillator analogous to the bacterial MinCDE system, at least one archaeal MinD exhibits pole-to-pole dynamics that are instead implicated in positioning the archaellum (the archaeal motility apparatus) and associated chemosensory arrays. This experimentally demonstrated functional re-wiring — MinD paralogues controlling organelle placement rather than septation — underscores how deviant Walker-type ATPases can be repurposed in archaeal cells. The example of *H. volcanii* therefore cautions against assuming functional equivalence between bacterial MinD and archaeal MinD homologues; instead, partner proteins and cellular context determine the operative role of each paralogue.

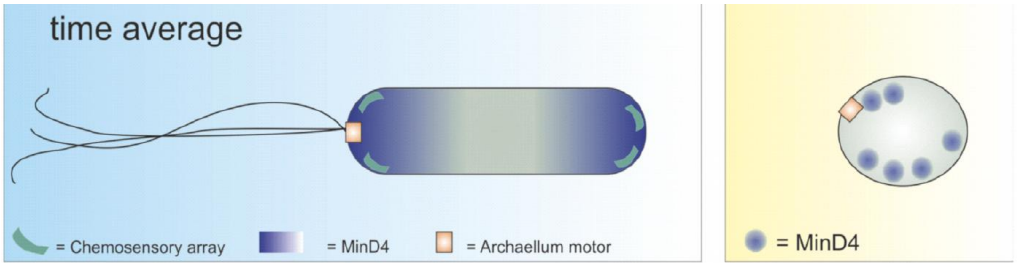

Figure 2: Time-averaged localization pattern of archaeal MinD4 in *H. volcanii*. Schematic representation of MinD4 distribution in rod-shaped and spherical *H. volcanii* cells. In both morphologies, MinD4 forms dynamic polar gradients and discrete foci that position chemosensory arrays and the archaellum motor, illustrating its role in spatial organization rather than divisome placement. (Figure adapted from Nußbaum et al., 2020)

Model organism 1: *Methanobrevibacter smithii*

M. smithii is the predominant archaeal methanogen in the human gut and the best-studied human-associated methanogen. It is an ovococcoid, Gram-positive, strict anaerobe assigned to the order Methanobacteriales and is frequently recovered from intestinal samples (and at lower frequency from oral and vaginal sites). As a dominant hydrogenotrophic methanogen in the human gut, *M. smithii* functions as a key hydrogen sink during microbial fermentation, potentially influencing host energy metabolism; however, evidence linking this activity to specific health or disease outcomes remains largely correlative (Samuel & Gordon, 2006; Gaci

et al., 2014). Importantly for cell-biological work, *M. smithii* currently lacks a genetic system, so mechanistic studies depend heavily on microscopy, biochemical reconstitution and structural approaches.

From a cell-envelope perspective *M. smithii* is noteworthy because members of Methanobacteriales (and Methanopyrales) are the only archaea to synthesize archaeal PG. As mentioned, *M. smithii* uses FtsZ1 and its anchor SepF for cell division. What are the other divisome components and how the FtsZ ring is placed remains currently unknown – *M. smithii* encodes multiple MinD-like proteins, but their roles has not been studied so far.

Model organism 2: *Methanopyrus kandleri*

M. kandleri is a phylogenetically deep-branching, hyperthermophilic methanogen originally isolated from deep-sea hydrothermal vents. It grows optimally at very high temperatures (usually around 98°C, but up to 121°C) and is notable for its adaptation to extreme environments (Kurr et al., 1991). Its complete genome was among the earliest archaeal genomes to be sequenced (Slesarev et al., 2002), revealing multiple features associated with hyperthermophilic adaptation, including pronounced amino acid composition bias, extensive DNA repair mechanisms, and protein stability signatures characteristic of growth at extreme temperatures.

Like Methanobacteriales, Methanopyrales are among the minority of archaeal groups that have an archaeal PG cell wall. The presence of a rigid PG wall implies that septal insertion and envelope remodelling must be coordinated with FtsZ (where present) in ways that may differ from S-layer-only archaeal systems, however, the division machinery of *M. kandleri* has not at all been experimentally characterized, in part because of the organism's extremophilic growth requirements and limited tractability. *M kanderli* encoders a single FtsZ1 homologue together with SepF which are likely involved in cell division, however, this still needs to be experimentally proven. Like all representatives of the Methanobacteriales and Methanopyrales, *M. kandleri* encodes several MinD-like homologues, but there functioning is unknown (Nußbaum et al., 2020).

Contextualization of the current knowledge into research hypothesis

The ParA/MinD-like family of ATPases (A/D ATPases) are proteins widespread across both bacteria and archaea and spatially organize an array of genetic- and protein-based cellular

cargos (Pulianmackal & Vecchiarelli, 2024) (Fig. 3A). Regardless of the cargo type, an ATPase cycle of ATP binding, protein dimer formation and ATP hydrolysis is key for the functioning of A/D ATPases (Pulianmackal & Vecchiarelli, 2024) (Fig. 3B). Bacterial MinD and ParA ATPases represent two distinct mechanistic paradigms: MinD is a membrane-bound ATPase that positions the FtsZ division ring, while ParA binds the nucleoid and drives ATP-dependent chromosome or cargo movement (Pulianmackal & Vecchiarelli, 2024) (Fig. 3C). Archaeal MinD homologs blur this classical distinction, e.g. archaellum positioning function of MinD4 from *H. volcanii*. *H. volcanii* MinD4 retained a membrane-targeting sequence typical of MinD and the oscillation pattern, yet it is not involved in FtsZ-ring placement (Nußbaum et al., 2020). The other *H. volcanii* MinD homologues are neither involved in cell division nor it is know if they are positioning any cellular cargos. This raises the central question of whether archaeal MinD operates in a bacterial MinD-like manner to regulate divisome positioning at all, or if it has a completely other functioning, e.g. in a ParA-like manner to influence nucleoid organization.

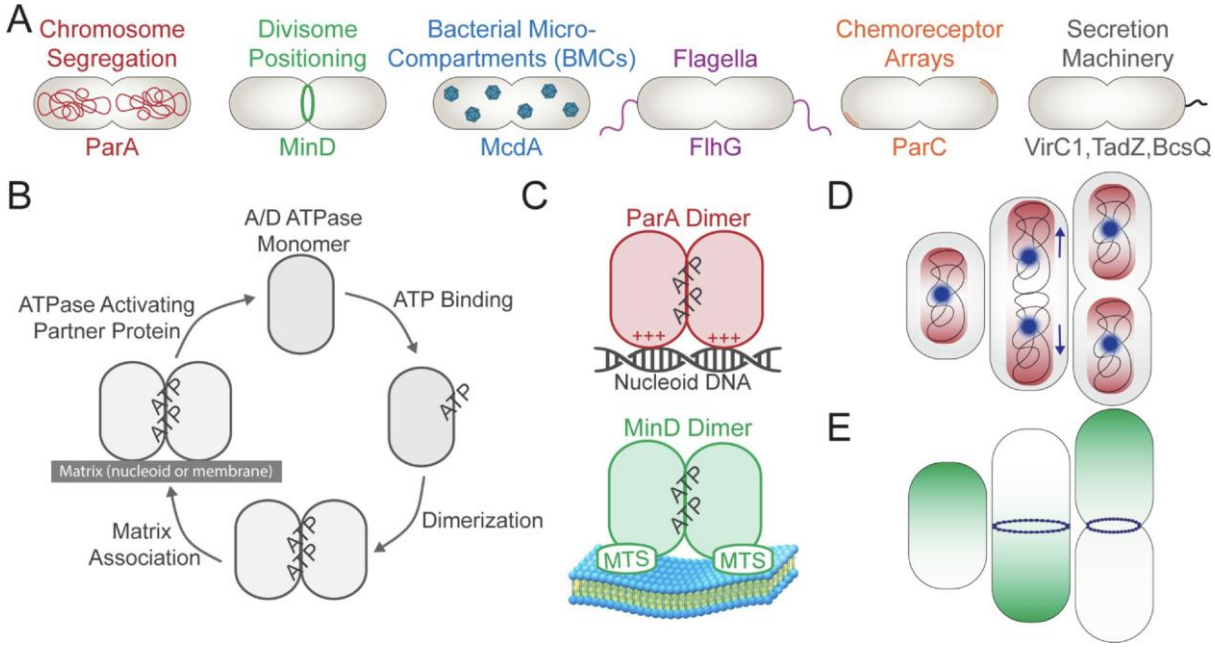

Figure 3: A/D family ATPases in bacteria.

(A) Cellular cargos (top) and the associated ATPases (bottom). (B) The ATPase cycle of A/D family ATPases. (C-E) Conceptual distinction between MinD-like and ParA-like ATPase mechanisms (from Pulianmackal & Vecchiarelli, 2024).

Comparative genomics shows that MinD is widespread but unevenly distributed across among Euryarchaeota as shown in Figure 1, occurring in many FtsZ-using lineages such as

Methanobacteriales, Methanopyrales and Halobacteriales, yet completely absent from other FtsZ-bearing groups (Ithurbide et al., 2022; Makarova et al., 2010). This patchy pattern indicates that MinD is not universally required for Z-ring positioning, unlike the bacterial MinCDE system**.**

Thus, although *M. smithii* and *M. kandleri* encode both FtsZ and MinD, evolutionary evidence cautions against assuming a strictly bacterial-like function and instead suggests that archaeal MinD may participate in broader spatial or chromosome-associated processes.

Therefore, my thesis focuses on two possible scenarios of MinD functioning in methanogenic archaea (Part 1):

Hypothesis 1: MinD from *M. smithii* and *M. kandleri* contributes to the positioning of the FtsZ-based division machinery in methanogenic archaea

This hypothesis proposes that archaeal MinD retains a function analogous to the bacterial Min system, guiding the spatial placement or maintenance of the FtsZ ring. *M. smithii* and *M. kandleri* both encode FtsZ and multiple homologues of MinD-like proteins. In these species, MinD, potentially with some other unknown proteins may act as a regulatory factor that positions or stabilizes FtsZ at midcell.

Hypothesis 2: MinD from *M. smithii* and *M. kandleri* is a DNA-binding ParA-like ATPase involved in chromosome segregation or DNA positioning

A second, equally plausible hypothesis arises from comparative analyses suggesting that many archaeal MinD-like proteins share significant sequence and mechanistic features with the broader A/D ATPase superfamily, raising the possibility that they may function more similarly to ParA-type DNA-associated ATPases than to canonical bacterial MinD regulators (Pulianmackal & Vecchiarelli, 2024). ParA ATPases are central components of DNA-segregation systems across bacteria and plasmids; they bind DNA in an ATP-dependent manner, form dynamic gradients on the nucleoid and drive the separation or positioning of chromosomal loci through self-organizing mechanisms (Vecchiarelli et al., 2014; Parker et al., 2021). Under this view, archaeal MinD might function not as a divisome-positioning factor but instead as a DNA-associated ATPase involved in organizing, segregating or structurally positioning the nucleoid.

Another, separate hypothesis that I am addressing in my thesis (in Part 2) is:

Hypothesis 3: SepF is the FtsZ-achor in *M. kandleri*

M. kandleri encodes both bacterial FtsZ-anchors, namely SepF and FtsA. In fact, most bacteria use FtsA as the FtsZ-anchor, in bacteria that have both, FtsA is the main anchor and SepF is dispensable, and in Actinobacteria and Cyanobacteria SepF is the FtsZ-anchor (Duman et al., 2013; Krol et al., 2012). While FtsZ and SepF widely cooccur in archaea, FtsA is exclusively found in Methanopyrales, with its only know representative *M. kandleri*. Due to the wide distribution of the FtsZ/SepF system in archaea and its conserved function between bacteria and archaea, it is tempting to assume that SepF is the main FtsZ-anchor in *M. kandleri*, while FtsA might fulfil another role.

Materials and Methods

M. smithii and *M. kandleri* Growth Conditions

M. smithii and *M. kandleri* were cultivated as closed batch cultures under strictly anaerobic conditions. Cultures were grown using a gaseous substrate mixture of molecular hydrogen and carbon dioxide (H_2/CO_2) containing 20 vol.% CO_2 in H_2. To maintain anaerobic conditions during medium preparation and autoclaving, a gas mixture of N_2/CO_2 (20 vol.% CO_2 in N_2) was used.

Cultivation was performed in 120 mL serum bottles sealed with crimped rubber stoppers. *M. smithii* cultures were incubated at 37°C with shaking at 120 rpm (Innova 44, New Brunswick Scientific, USA), whereas *M. kandleri* cultures were incubated at 98°C in a circulating water bath filled with oil with agitation at 140 rpm (Water Bath Circulating 22 L, Hach, USA). For both organisms, cultures were pressurized to 2 bar with H_2/CO_2 to sustain methanogenic growth.

Growth was monitored daily by measuring gas consumption using a manometer (LEO 1, Keller, Switzerland). Optical density measurements were also recorded to qualitatively monitor culture growth and consistency over time. Culture quality and cell morphology were regularly assessed by phase-contrast microscopy using an Eclipse Ni-L microscope (Nikon, Japan). To maintain cultures in exponential growth for downstream applications, including immunolabelling experiments, serial transfers were performed every few days. Excess cultures not used for transfers were stored at 4°C as backup stocks. To support the growth of archaeal

cultures, sterile stock solutions of trace elements and vitamins were prepared as described below for the media.

Trace Element Solution (1× TE Solution)

The trace element (TE) solution was prepared in 1 L of distilled water. Initially, 1.5 g of nitrilotriacetic acid was dissolved in approximately 800 mL of distilled water. The pH was adjusted to 6.5 using potassium hydroxide (KOH) to facilitate dissolution. Subsequently, the following components were added sequentially with constant stirring: 3 g $MgSO_4 \cdot 7H_2O$, 0.585 g $MnCl_2 \cdot 4H_2O$, 1 g NaCl, 0.1 g $FeSO_4 \cdot 7H_2O$, 0.18 g $CoSO_4 \cdot 7H_2O$, 0.1 g $CaCl_2 \cdot 2H_2O$, 0.18 g $ZnSO_4 \cdot 7H_2O$, 0.006 g $CuSO_4$, 0.02 g $KAl(SO_4)_2 \cdot 12H_2O$, 0.01 g H_3BO_3, 0.01 g $Na_2MoO_4 \cdot 2H_2O$, 0.03 g $NiCl_2 \cdot 6H_2O$, 0.0003 g $Na_2SeO_3 \cdot 5H_2O$, and 0.0004 g $Na_2WO_4 \cdot 2H_2O$. After complete dissolution of all salts, the final pH was adjusted to 7.0 using KOH. The solution was then made up to 1 L with distilled water. The TE solution was aliquoted into sterile containers, autoclaved and stored at room temperature.

Vitamin Solution

A 1 L vitamin solution was prepared by dissolving the following components in approximately 800 mL of distilled water: 0.002 g biotin, 0.002 g folic acid, 0.01 g pyridoxine-HCl, 0.005 g thiamine-HCl·$2H_2O$, 0.005 g riboflavin, 0.005 g nicotinic acid, 0.005 g D-calcium pantothenate, 0.1 mg vitamin B_{12}, 0.005 g p-aminobenzoic acid, and 0.005 g lipoic acid. The solution was mixed until all components were completely dissolved. The final volume was adjusted to 1 L with distilled water. The vitamin solution was sterilized by filtration using a 0.22 µm filter and stored at 4 °C in the dark.

Preparation of Methanobrevibacter Medium

M. smithii was cultured in adapted DSMZ 141, methanogen medium as described in (Pende & Sogues et al., 2021). The base medium contained the following components per 1000 mL: 0.34 g KCl, 4 g $MgCl_2 \cdot 6H_2O$, 0.25 g NH_4Cl, 0.14 g $CaCl_2 \cdot 2H_2O$, 0.14 g K_2HPO_4, 3.45 g $MgSO_4 \cdot 7H_2O$, 6 g NaCl, 1 g sodium acetate, 2 g yeast extract, 5 g $NaHCO_3$, and 0.5 g L-cysteine. These components were initially dissolved in 480 mL of double-distilled water (ddH_2O).

To this base, the following additives were included: 10 mL of TE solution, 1 mL of $Fe(NH_4)_2(SO_4)_2 \cdot 6H_2O$ solution, 100 µL of 0.7 mg mL^{-1} sodium resazurin solution, and 10 mL

of a vitamin solution. Finally, the pH was adjusted to 7 and the volume was filled up to 1000 mL with ddH_2O.

50 mL of the medium was transferred to 120 mL serum bottles, sealed with rubber stoppers (pretreated by boiling ten times for 30 min in fresh ddH_2O; 20mm, butyl rubber, CLS-3409-14, Chemglass Life Sciences) and sealed with crimp caps (20 mm aluminum, Ochs Laborbedarf, Bovenden, Germany). The medium was flushed with an N_2CO_2 gas mixture, and then autoclaved. Following sterilization, 0.2 mL of 0.6M Na_2S was added anaerobically to each bottle using a syringe. The medium was flushed with 20 Vol.-% CO_2 in H_2 (H_2/CO_2).

Cultures were incubated at 37 °C with shaking at 120 rpm. To maintain anaerobic conditions and ensure sufficient substrate availability, the bottles were re-gassed with a 20 Vol.-% CO_2 in H_2 (H_2/CO_2) at 2 bar overpressure daily.

The methanogenic reaction that supports *M. smithii* growth is as follows:

$4H_2+CO_2 \rightarrow CH_4+2H_2O$

Preparation of Methanopyrus Medium

The Methanopyrus growth medium was prepared by dissolving the following components in distilled water: 0.25 g NH_4Cl, 0.07 g $K_2HPO_4 \cdot 3H_2O$, 0.09 g KH_2PO_4, 11.80 g NaCl, 1.75 g $MgSO_4 \cdot 7H_2O$, 4.50 g $MgCl_2 \cdot 6H_2O$, 0.81 g Na_2SO_4, 0.78 g $CaCl_2 \cdot 2H_2O$, 0.30 g KCl, and 1g $NaHCO_3$. The total volume was made up to 970 mL with distilled water.

To this base solution, 10 mL of TE solution (see above) was added, along with 2 mL each of 0.1% (w/v) $(NH_4)_2Fe(SO_4)_2 \cdot 6H_2O$, 0.1% (w/v) $(NH_4)_2Ni(SO_4)_2$, and 0.1% (w/v) $Na_2WO_4 \cdot 2H_2O$. Additionally, 10 mL of marine trace element solution (see below) and 0.5 mL of 100 µL of 0.7 mg mL^{-1} sodium resazurin solution were added.

50 mL of the medium was transferred to 120 mL serum bottles, sealed with rubber stoppers (pretreated by boiling ten times for 30 min in fresh ddH_2O; 20mm, butyl rubber, CLS-3409-14, Chemglass Life Sciences) and sealed with crimp caps (20 mm aluminum, Ochs Laborbedarf, Bovenden, Germany). The medium was flushed with an N_2CO_2 gas mixture, and then autoclaved. Following sterilization, 0.2 mL of 0.6M Na_2S was added anaerobically to each bottle using a syringe. The medium was flushed with 20 Vol.-% CO_2 in H_2 (H_2/CO_2). If necessary, the pH was adjusted to 6.5 using sterile, anoxic acid or base solutions.

Cultures were incubated at 98 °C with shaking at 120 rpm. To maintain anaerobic conditions and ensure sufficient substrate availability, the bottles were re-gassed with a 20 Vol.-% CO_2 in H_2 (H_2/CO_2) at 1 bar overpressure daily.

Marine Trace Element Solution

To prepare the marine trace element solution, 4.00 g NaBr, 1.80 g $SrCl_2 \cdot 6H_2O$, and 1.30 g H_3BO_3 were dissolved in distilled water. To this, 1.25 mg KI, 100 mg of sodium silicate, 60 mg NaF, 40 mg KNO_3, and 0.25 mg $Na_2HPO_4 \cdot 3H_2O$ were added. The final volume was adjusted with distilled water to 1 liter, and the solution was autoclaved before use.

ATPase Activity Assay

ATP hydrolysis by *M. smithii* and *M. kandleri* MinD proteins was quantified using the EnzChek Phosphate Assay Kit (Thermo Fisher Scientific, USA), which detects inorganic phosphate release through a coupled MESG/purine nucleoside phosphorylase (PNP) colorimetric reaction measured at 360 nm (Webb, 1992; Thermo Fisher Scientific, EnzChek Phosphate Assay Kit Manual). All reactions were performed in flat-bottom 96-well microplates in a final volume of 200 µL. Standard assay mixtures contained 1× assay buffer supplied with the kit, 1 mmol L^{-1} $MgCl_2$, and MESG and PNP at concentrations recommended by the manufacturer. Purified MinD proteins or SepF (negative control) were added to the reaction mixture and equilibrated for 2–5 min at room temperature prior to reaction initiation.

Reactions were initiated by addition of ATP to a final concentration of 1 mmol L^{-1}, after which plates were immediately transferred to a microplate spectrophotometer (UV-Star microplate, Greiner Bio-One, Germany) pre-equilibrated at room temperature. Absorbance at 360 nm was recorded continuously at 5 s intervals for 300 s. Each assay plate included buffer-only blanks, ATP-only controls, protein-only controls, and SepF + ATP negative controls to account for background signal and non-enzymatic phosphate release.

A phosphate calibration series (0–100 µmol L^{-1}) was prepared in parallel on the same plate, and absorbance values from the standards were fitted linearly to generate a standard curve. The 100 µmol L^{-1} standard was excluded due to signal saturation. Raw absorbance traces were baseline corrected using protein-only controls and converted to phosphate concentrations using the calibration curve.

Western Blot Analysis

For protein extraction, 2 mL of *M. smithii* or *M. kandleri* cultures were harvested by centrifugation (Eppendorf, centrifuge 5420) at 8,000 x g for 5 min. The supernatant was discarded, and the cell pellet was resuspended in 200 µL of phosphate buffered saline (PBS). Approximately 100µL of sterile glass beads were added to each sample in a 1.5 mL screw cap tube, and cells were lysed using a bead beater (program: 4 ms^{-1}, 30 sec with 1 min break, 3X bread beating) to ensure efficient mechanical disruption of the archaeal cell walls.

Following lysis, the tubes were briefly centrifuged, and the supernatant containing soluble proteins was transferred to a fresh tube. To each sample, 25 µL of 4X LDS sample buffer (or Roti-Load) and 0.25 µL of 1 M dithiothreitel (DTT) were added. In the case of purified protein samples, proteins were diluted accordingly before the addition of LDS and DTT.

Both whole cell lysates and purified protein samples were denatured by boiling at 95 °C for 5 min prior to SDS PAGE analysis. Whole cell lysate and purified protein samples (15 - 30 µL) were loaded onto a 4 - 12% Tris Glycine SDS-PAGE gel for electrophoresis. The inner chamber was filled with 1X Tris running buffer (50 mmol L^{-1} Tris, 384 mmol L^{-1} glycine, 0.1% SDS, pH 8.3) and electrophoresis was performed at 150 V for 50 - 60 min.

Following electrophoresis, the gel was removed, trimmed, and rinsed briefly in water. For protein transfer, Whatman paper and nitrocellulose membrane were soaked in water followed by transfer buffer (25 mmol L^{-1} Tris, 192 mmol L^{-1} glycine, 20% methanol, 0.1% SDS, pH 8.3). Protein transfer was carried out at 100 V for 1 h.

After transfer, membranes were stained with Ponceau S solution for 2 - 5 min to verify protein transfer and then rinsed in water. Membranes were marked, washed in PBS, and blocked in 5% non-fat dry milk prepared in PBST (1X PBS with 0.1% Tween 20) for 45 min at room temperature.

Primary antibody (1:500 dilution) incubation was carried out overnight at 4°C in PBS-T containing 5% milk. After washing the membrane three times with PBS-T for five min, it was incubated with HRP conjugated secondary antibodies diluted 1:5000 in blocking buffer for 1 h at room temperature. Following additional three washes in PBS-T and a final was in PBS, chemiluminescent detection was performed using ECL reagents (NeoPRO Pico Ultra (Pico kit), Neo Biotech Co., Ltd., South Korea). The membrane was incubated with the mixed

substrate for 1 min before imaging using an iBright imaging system (Invitrogen by Thermo Fisher Scientific, USA).

Immunolabeling

M. smithii cells were grown to an OD_{578} of 0.3 and 2 mL of culture were harvested by centrifugation (Eppendorf, centrifuge 5420) at 3381 x g for 2 min. All subsequent centrifugation steps were performed at the same speed unless otherwise stated. The cell pellets were washed once in 1 mL of PBS, pelleted again, and fixed in 80% ice-cold methanol for 10 min on ice.

Fixed cells were rehydrated and washed in 50 mmol L^{-1} HEPES buffer (pH 7.0). Permeabilization was performed by incubating the cells for 10 min at 71 °C in 100 µL of 50 mmol L^{-1} HEPES buffer containing 1.42 mg mL^{-1} of purified endoisopeptidase PeiW and 1 mmol L^{-1} DTT. Following this, cells were cooled on ice for 2 min, pelleted, and washed once in 50 mmol L^{-1} HEPES buffer and twice with PBS-T (1× PBS supplemented with 0.1% v/v Tween-20).

Blocking was carried out for 1 h at room temperature in PBS-T containing 2% (w/v) bovine serum albumin (BSA). Cells were then incubated overnight at 4 °C with a 1:200 dilution of either anti-*M. smithii* FtsZ and/or MinD antibody, and anti-*M. kandleri* FtsZ, MinD and/or SepF antibody - depending on the organism - in blocking solution.

The next day, cells were washed three times in PBS-T and incubated for 1 h at room temperature in the dark with fluorophore-conjugated secondary antibodies: for *M. smithii* anti-rabbit Alexa Fluor 555 for FtsZ, and anti-rat Alexa Fluor 488 for MinD at a 1:500 dilution in PPS-T. Prior to incubation, secondary antibodies were centrifuged briefly to remove unconjugated fluorophores. Non-specific binding was removed by two washes in PBS-T and one final wash in PBS. Labeled cells were resuspended in 20 µL of PBS.

The same protocol was applied to *M. kandleri* cells with one modification: due to the soft and fragile nature of *M. kandleri* cell pellets, all centrifugation steps were extended to 5 min. Additionally, immunolabeling with anti-SepF (detected using anti-rat Alexa Fluor 488), with anti-MinD (detected using anti-chicken Alexa Fluor 488) was performed in combination with anti- FtsZ (detected using anti-rabbit Alexa Fluor 555) labeling to assess co-localization in *M. kandleri*. For DNA visualization, the cell pellets were resuspended in 1:1000 Hoechst dye

diluted in PBS and incubated in the dark for 10 min. Cells were then washed once with PBS, mounted on microscope slides, and imaged immediately using fluorescence microscopy.

For microscopy, 2 µL of cell suspension was mixed with 1 µL of Vectashield mounting medium (Vector labs) and applied onto microscope slides coated with 1% agarose. A coverslip was gently placed over the sample, and cells were visualized using Nikon Eclipse epifluorescence microscopy with a 100X Objective.

Image Analysis of *M. smithii* and *M. kandleri*

Images were processed using Fiji (ImageJ) Version 2.0.0-rc-68/1.54p in combination with plugin MicrobeJ. MicrobeJ is a Fiji/ImageJ plugin for high-throughput bacterial cell detection and quantitative analysis (Ducret et al., 2016). Phase-contrast and fluorescence images of immunolabelled *M. smithii* and *M. kandleri* cells were imported into MicrobeJ, where channels and spatial scales were defined. Automatic cell detection was performed using size and shape-based parameters tailored to each organism, and out-of-range objects were excluded. Fluorescence maxima were identified by adjusting signal tolerance thresholds for each marker (MinD, FtsZ, SepF) to minimize background. The cell outlines were traced and cell length, width, fluorescence intensity along the cell length and presence of fluorescent maxima were measured automatically. Cells were manually curated to retain well-stained, morphologically intact cells. The resulting datasets were used to generate cell length distributions, fluorescence intensity profiles and subcellular localization density maps, enabling comparison of protein localization across division stages. For the plots showing the relative position of detected maxima, cells were automatically grouped into three size classes.

Electrophoretic Mobility Shift Assay (EMSA)

Electrophoretic mobility shift assays (EMSAs) were performed to examine the DNA-binding activity of MinD. Protein concentrations (blank: 50 mmol L^{-1} HEPES, 150 mmol L^{-1} NaCl, 5% glycerol) and DNA concentrations (blank: nuclease-free water) were quantified using a NanoDrop spectrophotometer (Nanophotometer N60 by IMPLEN, Germany). Working dilutions of purified MinD (1:10 and 1:200) were prepared in protein low-bind tubes, whereas DNA was diluted 1:10 in DNA low-bind tubes.

The reactions were assembled in protein low-bind tubes to a final volume of 20 µL containing PBS. The DNA concentration was kept constant at 30 ng per reaction. Protein was added at increasing concentrations (0–200 µmol L^{-1}). Negative controls included BSA (50 µmol L^{-1}) and heat-inactivated MinD. Heat inactivation was performed by incubating the highest MinD concentration in 1× PBS supplemented with 1 mmol L^{-1} DTT and 0.02% SDS at 99 °C for 10 min, followed by immediate cooling on ice. As a positive control for DNA binding, the archaeal chromatin protein Alba (25 µmol L^{-1}) was included. *E. coli* MinD at 200 µmol L^{-1} was used as a second negative control.

Reaction mixtures were incubated for 30 min at room temperature (20 °C). Following incubation, 3 µL of 6× loading dye (10 mmol L^{-1} Tris-HCl, pH 7.6; 1.5 mg/mL Orange G; 60% glycerol) was added, and samples (23 µL) were loaded onto a 1% native agarose gel prepared in 1× TAE buffer. Electrophoresis was performed at 100 V for 45 min at room temperature.

After electrophoresis, gels were post-stained with SYBR green (Thermo Fisher Scientific, USA) for 20 min in the dark with gentle agitation. DNA–protein complexes were visualized using the gel documentation system iBright 1500 (Invitrogen by Thermo Fisher Scientific, USA) under blue-light illumination.

Co-Immunoprecipitation (Co-IP) of MinD from *M. smithii* and *M. kandleri*

Co-IP was used to isolate MinD and its potential interaction partners from *M. smithii* and *M. kandleri* using antibody-coupled resin (for IgY-based antibodies) or magnetic beads (for IgG-based antibodies). All experiments were performed in biological triplicates for *M. kandleri* and in duplicates for *M. smithii*, including appropriate antibody controls (IgY for *M. kandleri* and IgG for *M. smithii*).

Cell culture, crosslinking, and harvesting

For each Co-IP reaction, 10 mL cultures of *M. smithii* and *M. kandleri* were collected during early exponential growth. To stabilize protein–protein interactions, cells were crosslinked directly in culture medium using freshly prepared 37% formaldehyde. A final concentration of 0.25% formaldehyde was achieved by adding 67.6 µL to each culture, followed by gentle agitation for 20 min at room temperature. Crosslinking was quenched by adding 1 mL of 2.5 mol L^{-1} glycine to a final concentration of 0.25 mol L^{-1}. Cells were harvested by centrifugation (Hettich Zentrifugen, Universal 320R) at 2,100 × g for 10 min at room temperature and

subsequently washed twice with 10 mL PBS and once with 1 mL PBS. Cell pellets were kept on ice until lysis.

Cell lysis and preparation of archaeal lysates

Cell pellets from both species were resuspended in 1.2 mL of freshly prepared Archaea Lysis (AL) Buffer. The AL buffer consisted of 50 mmol L^{-1} Tris-HCl (pH 7.4), 150 mmol L^{-1} NaCl, 10 mmol L^{-1} $MgCl_2$, 1 mmol L^{-1} EDTA, and 0.1% IGEPAL CA-630, prepared in Milli-Q water to a final volume of 50 mL. Before use, the buffer was supplemented with 1 mmol L^{-1} DTT and 25× protease inhibitor solution (40 µL mL^{-1}) prepared by dissolving one tablet(cOmplete EDTA free, Roche Diagnostics GmbH, Mannheim, Germany) in 2 mL of water. Lysis was performed by sonication using the settings previously optimized for archaeal CoIP experiments (sonication with a 220-B head, 1 sec on/3 sec off pulses for a total of 7 min at 20% amplitude) (Sonicator Dismembrator Q700 – Fisherbrand – Fisher Scientific, part of Thermo Fisher Scientific, USA). Lysates were clarified by centrifugation at 16,000 × g (Eppendorf, Centrifuge 5415R) for 20 min at 4°C, and the cleared supernatants were used for overnight incubation with antibody-coupled resin or magnetic beads at 4°C (see below).

Antibody coupling for M. kandleri (IgY) using AminoLink Plus Resin

Antibodies targeting *M. kandleri* MinD or control chicken IgY were covalently coupled to AminoLink Plus Resin following the manufacturer's protocol (Pierce Co Immunoprecipitation kit by Thermo Scientific, USA) with minor modifications. Resin slurry (25 µL per IP) was equilibrated twice with 1× Coupling Buffer. Antibodies were diluted 1:1 in glycerol, so accordingly the antibody was added before coupling to achieve 10 µg antibody per reaction. MinD-specific antibody (3.6 µL of a 5.55 mg mL^{-1} stock, diluted to 2.78 mg mL^{-1}) and control IgY (20 µL of a 1 mg mL^{-1} stock) were mixed with resin in a final volume of ~200 µL. Coupling was initiated by adding sodium cyanoborohydride and incubated for 2 h at room temperature. Unreacted aldehyde groups were quenched using Quenching Buffer containing $NaCNBH_3$ for 30 min. Resin samples were subsequently washed three times with Wash/Lysis Buffer provided in the kit.

After coupling, 500 µL of archaeal lysate (prepared as described above) was added to each resin sample and incubated overnight at 4°C on a rotating wheel.

Antibody coupling for M. smithii (IgG) using Protein G Magnetic Beads

For *M. smithii* samples, rabbit IgG-based anti-MinD antibodies and control IgG were crosslinked to Protein G magnetic beads (Pierce Crosslink Magnetic IP/CoIP kit by Thermo Scientific, USA). Antibodies were diluted to achieve 10 µg per 100 µL reaction using a mixture of 20× Coupling Buffer and IP Lysis/Wash Buffer. MinD antibody (102 µL of a 196 µg mL^{-1} stock, diluted to 98 µg mL^{-1} effective concentration) and control rabbit IgG (10 µL of 1 mg mL^{-1} stock) were prepared in reaction volumes adjusted to 100 µL with ultrapure water.

DSS (disuccinimidyl suberate) crosslinker was freshly prepared by dissolving a single DSS capsule in 217 µL DMSO to generate a 25 mmol L^{-1} stock. This stock was diluted 1:100 in DMSO to yield a 0.25 mmol L^{-1} working solution. Magnetic beads (25 µL per IP) were washed in 1× Modified Coupling Buffer and incubated with the prepared antibody solution for 15 min at room temperature on a rotating platform. After washing, a DSS-containing crosslinking mixture was added and incubated for 30 min to covalently crosslink antibodies to the beads. The magnetic beads were washed repeatedly with elution buffer to remove unbound antibody and subsequently equilibrated twice in AL buffer or stored at 4°C. Following equilibration, 500 µL of archaeal cell lysate (prepared as described above) was added to each bead sample and incubated overnight at 4°C on a rotating wheel to allow protein–antibody binding.

Washing and elution

Following overnight incubation, immune complexes were collected by centrifugation (resin) or magnetic separation (beads). Samples were washed twice with 500 µL cold AL buffer to remove loosely bound proteins. A final wash was performed using No-Detergent (ND) Buffer, which consisted of 20 mmol L^{-1} Tris-HCl (pH 7.5) and 75 mmol L^{-1} NaCl, prepared to a final volume of 15 mL with Milli-Q water. ND buffer minimized detergent carryover. After the final wash, the beads and resin were kept on ice and no elution step was performed. Instead, the bead- or resin-bound protein complexes were processed directly for mass spectrometry sample preparation using the PreOmics iST sample preparation kit (PREOMICS, Germany), according to the manufacturer's instructions. This approach was chosen to minimize sample loss and to ensure sufficient material for downstream analysis. Prepared samples were submitted to the mass spectrometry facility at UBB, Djerassiplatz 1, 1030 Vienna (3rd floor, Rooms 3.062/3.066), where measurements were performed by Dr. Leila Afjehi and her team.

Result Part 1: Function of MinD in *M. smithii* and *M. kandleri*

Archaeal and bacterial MinD show strong sequence conservation

A multiple sequence alignment of MinD homologs from representative bacteria and archaea was generated, with bacterial sequences grouped at the top and archaeal sequences grouped below, including *M. smithii* and *M. kandleri* highlighted at the bottom of the alignment (Fig. 4) which was designed by Dr. Nika Pende. The alignment reveals strong conservation of the core P-loop NTPase architecture across all sequences analyzed. In particular, the canonical Walker A motif (GxxxxGKST), required for ATP binding, and the Walker B motif, required for ATP hydrolysis, are fully conserved in both bacterial and archaeal MinD proteins, consistent with their classification within the deviant Walker-type ParA/MinD ATPase family (Hu & Lutkenhaus, 1999; Szardenings et al., 2011; Nußbaum et al., 2020).

Sequence conservation is indicated using standard alignment notation: asterisks (*) denote identical residues, colons (:) indicate conserved substitutions with similar physicochemical properties, and dots (.) represent semi-conserved substitutions. This pattern highlights a highly conserved ATPase core flanked by more variable regions, particularly toward the N-terminus. Secondary-structure predictions are overlaid on the alignment, with α-helical regions indicated in red and β-strands in blue; colour intensity reflects the confidence of the prediction, with darker shading corresponding to higher confidence.

In addition to the conserved ATPase core, a putative C-terminal membrane-targeting sequence (MTS) is evident in both bacterial and archaeal MinD homologs and is highlighted by full or dashed boxes in the alignment (Fig. 4). In bacterial MinD, this amphipathic helix mediates membrane association and is essential for spatial regulation of MinD activity (Hu & Lutkenhaus, 1999; Lutkenhaus, 2007). The presence of a similarly positioned and compositionally conserved region in *M. smithii*, *M. kandleri*, and *Haloferax volcanii* MinD suggests that archaeal MinD proteins retain the biochemical capacity for membrane interaction. For *H. volcanii* MinD4, only the region encompassing the conserved MTS is shown; the remaining C-terminal sequence was omitted from the alignment due to its extended length, which is indicated by a break (//) in the sequence.

By contrast, the N-terminal regions show greater sequence divergence. Notably, *M. smithii* MinD contains an extended N-terminal segment relative to *M. kandleri*, *H. volcanii*, and bacterial homologs. Despite this variability, the alignment demonstrates that archaeal MinD

proteins preserve all defining structural and biochemical features of MinD/ParA ATPases, including conserved ATP-binding motifs and a C-terminal membrane-targeting region. Together, these data support strong evolutionary conservation at the level of ATPase function while allowing for lineage-specific adaptations that may underlie functional divergence in archaeal MinD proteins (Nußbaum et al., 2020; Pulianmackal & Vecchiarelli, 2024).

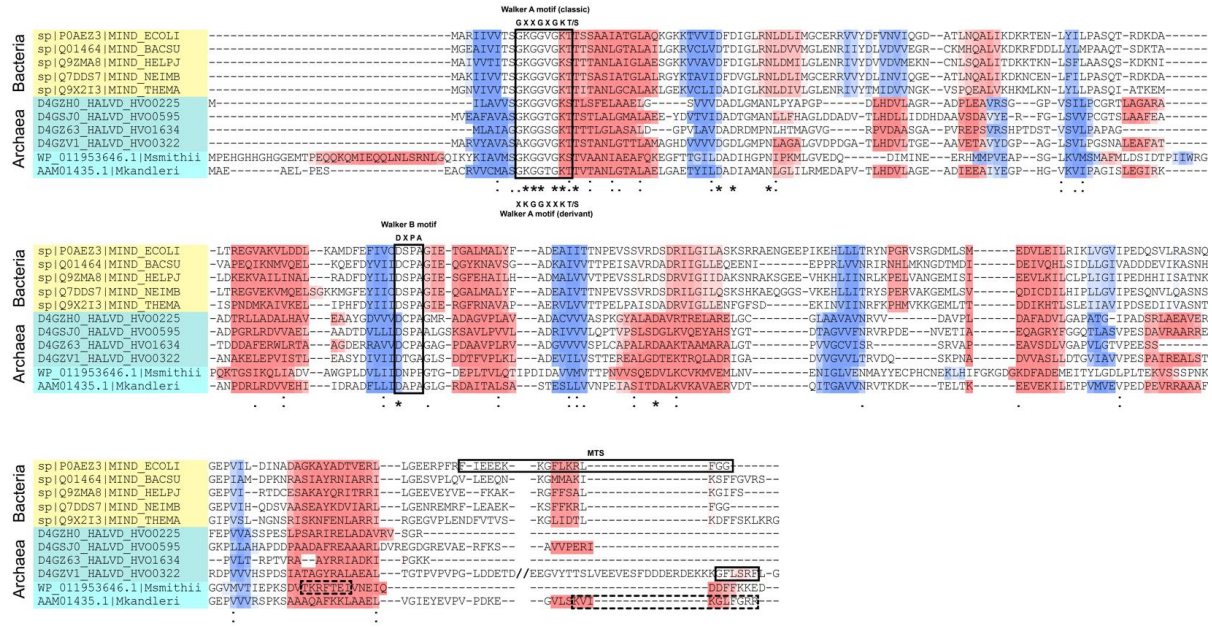

Figure 4: Multiple sequence alignment of bacterial and archaeal MinD homologs, produced by Dr. Nika Pende. Amino acid alignment of MinD proteins from representative bacterial and archaeal species. Identical residues across all sequences are indicated by an asterisk (*). Conserved substitutions, representing amino acids with similar physicochemical properties (predominantly hydrophobic residues), are denoted by a colon (:), while semi-conserved substitutions are indicated by a period (.). These symbols highlight the degree of sequence conservation underlying the shared structural and functional features of MinD/ParA-family ATPases.

MinD from Methanogenic Archaea has ATPase Activity

To determine whether MinD from methanogenic archaea exhibits ATPase activity, purified MinD proteins from *M. smithii* and *M. kandleri* were analysed using a continuous phosphate-detection assay based on enzymatic detection of inorganic phosphate release (Webb, 1992). All reactions were performed in technical duplicates and included multiple control conditions to validate assay specificity.

MinD from both organisms showed a clear, time-dependent increase in phosphate production following ATP addition (Fig.5). Wells containing *M. smithii* MinD with ATP (Ms MinD +ATP – Ms MinD + ATP rep) displayed a pronounced and rapid increase in signal, consistent with robust ATP hydrolysis. *M. kandleri* MinD with ATP (Ms MinD +ATP – Ms MinD + ATP rep) also exhibited ATPase activity, although with a slower apparent rate and lower overall phosphate accumulation compared to *M. smithii* MinD. The observed ATPase activity is consistent with the known biochemical properties of ParA/MinD-family ATPases, which hydrolyze ATP as part of their functional cycle (Leonard et al., 2005; Vecchiarelli et al., 2010).

None of the control reactions showed measurable ATPase activity. Blank wells (C1–C2) remained at baseline throughout the measurement period. Protein-only controls for *M. smithii* MinD (C3–C4), *M. kandleri* MinD (C5–C6), and SepF (C7–C8) showed no detectable phosphate release in the absence of ATP. Furthermore, SepF incubated with ATP (D1–D2), included as a non-ATPase negative control, did not produce detectable phosphate, confirming that the observed activity was specific to MinD.

Together, these results demonstrate that MinD from both *M. smithii* and *M. kandleri* is an active ATPase. Under the assay conditions used, *M. smithii* MinD exhibited higher apparent ATPase activity than *M. kandleri* MinD. Importantly, all measurements were performed at room temperature, which is close to the optimal growth temperature of *M. smithii* but far below the physiological growth temperature of the hyperthermophilic archaeon *M. kandleri*. Increasing the reaction temperature toward physiological conditions may enhance the ATPase activity of *M. kandleri* MinD and provide a more accurate comparison of enzymatic kinetics between the two species.

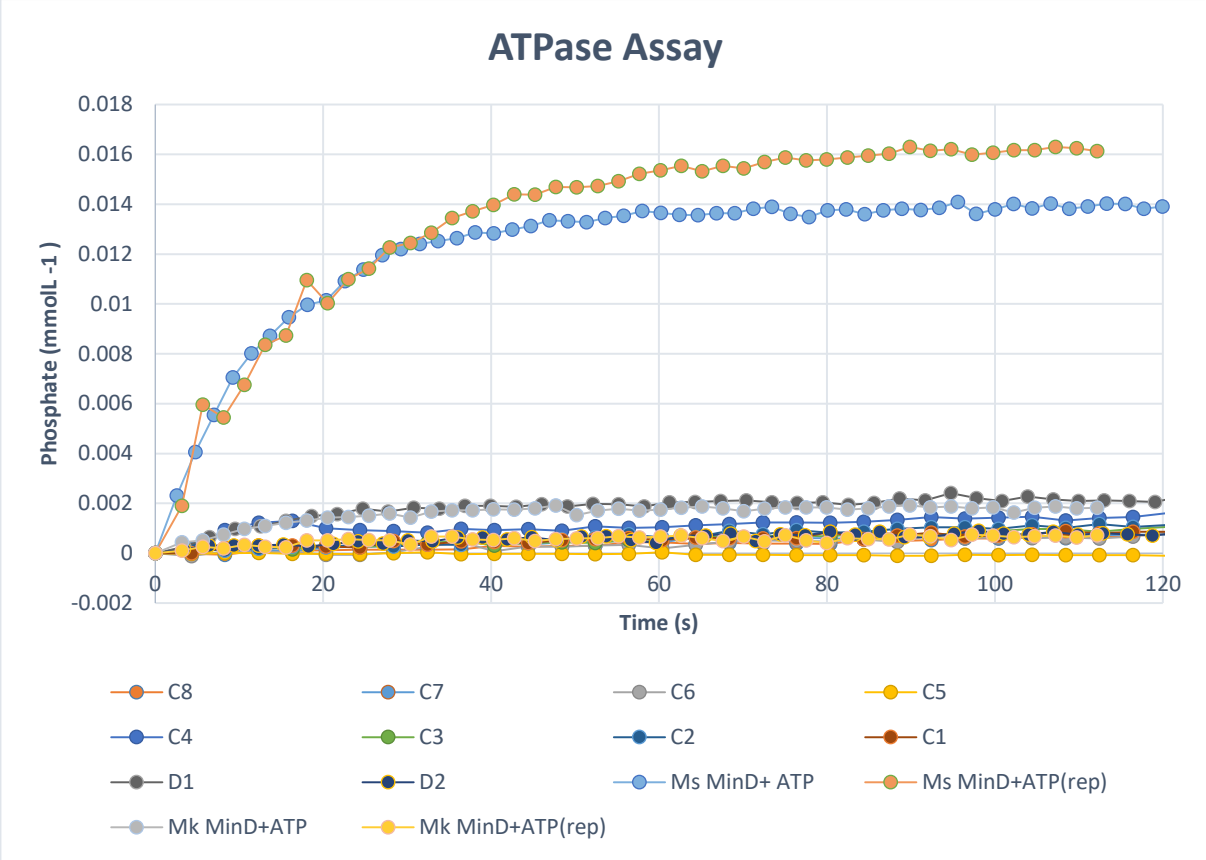

Figure 5: ATPase activity of MinD from *M. smithii* and *M. kandleri*.

Time-course of inorganic phosphate production during ATP hydrolysis by purified MinD proteins from *M. smithii* (Ms MinD + ATP; two technical replicates) and *M. kandleri* (Mk MinD + ATP; two technical replicates), monitored using the EnzCheck MESG/PNP assay. Phosphate concentration (mmol L^{-1}) is plotted as a function of time (s). Ms MinD shows a rapid and pronounced increase in phosphate release, indicating robust ATPase activity, whereas Mk MinD displays a slower and weaker increase under the same assay conditions. Control reactions (C1–C8, D1–D2), including buffer-only, protein-only and SepF + ATP, remain at baseline, confirming that phosphate production is specific to MinD-dependent ATP hydrolysis.

M. kandleri and *M. smithii* express FtsZ and MinD

Western blot analysis was performed to assess the expression of FtsZ and MinD and to validate antibody specificity using purified proteins and whole-cell lysates from *M. kandleri* (Mk) and *M. smithii* (Ms) (Fig.6). Lane 1 contains the molecular weight marker.

For FtsZ, a strong and distinct band corresponding to the purified *M. kandleri* protein (~43 kDa) was detected (lane 3), consistent with the expected molecular weight of archaeal FtsZ (Pende & Sogues et al., 2021; Wagstaff & Löwe, 2018). In contrast, the *M. kandleri* whole-cell lysate (lane 2), showed only weak signal that became apparent upon longer exposure. In the *M. smithii* lysate (lane 8), a clear FtsZ signal was observed at ~40 kDa, consistent with previous reports for methanogenic archaea (Pende & Sogues et al., 2021).

For MinD, purified *M. kandleri* MinD (lane 5) produced a faint band at ~30 kDa, which became visible upon overexposure but was consistent with the predicted molecular weight of archaeal MinD proteins (Nußbaum et al., 2020). In *M. kandleri* whole-cell lysates (lane 4), MinD appeared as a strong smear which seems to be oversaturated upon exposure. In contrast, *M. smithii* MinD was readily detected in whole-cell lysates (lane 6) and the purified Ms MinD protein (lane 9) yielded a clear band at ~32 kDa after longer exposure.

Taken together, these results confirm the specificity of the antibodies and demonstrate detectable expression of FtsZ and MinD in both methanogenic species.

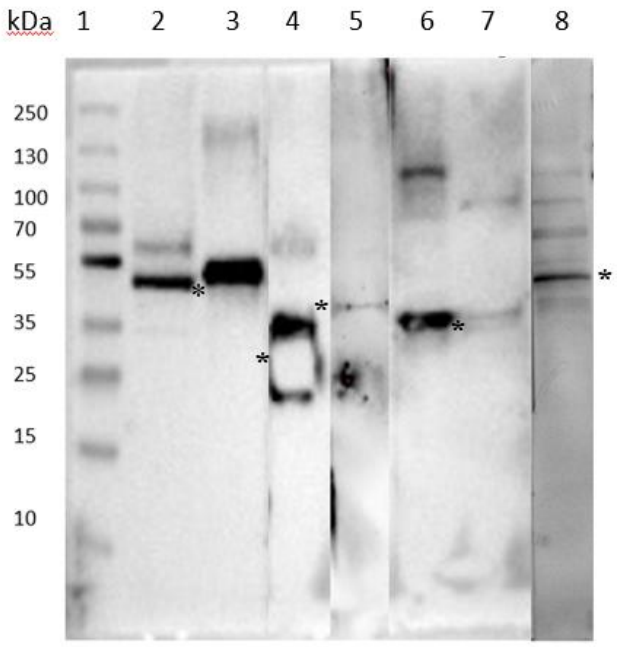

Figure 6: Western blot analysis of FtsZ, and MinD in *M. kandleri* (Mk) and *M. smithii* (Ms). (*) indicates the protein band corresponding to the expected size.

Whole-cell lysates and purified proteins were analyzed by SDS–PAGE followed by Western blotting. Lane 1: protein ladder; Lanes 2–3: *M. kandleri* cell lysate and purified FtsZ (primary anti-FtsZ, 1:500; secondary anti-rabbit, 1:5000); Lanes 4–5: *M. kandleri* cell lysate

and purified MinD (primary anti-MinD, 1:500; secondary anti-chicken, 1:5000); Lanes 6–7: *M. smithii* lysate and purified MinD (primary anti-MinD, 1:500; secondary anti-rat, 1:1000); Lane 8: *M. smithii* lysate of FtsZ. The expected molecular weights were: MkFtsZ (43 kDa), MkSepF (13 kDa), MkMinD (28.5 kDa), MsMinD (31.9 kDa), and MsFtsZ (39.8 kDa).

M. smithii and *M. kandleri* MinD partially co-localized with FtsZ

Immunolabelling was performed in *M. smithii* and *M. kandleri* using an anti-MinD antibody, either alone or in combination with an anti-FtsZ antibody. FtsZ staining served as a positive control for successful immunolabelling and as a marker of the division plane, as its localization in *M. smithii* has been previously described (Pende & Sogues et al., 2021). The immunolabelling protocol was adapted from established methods for methanogens and optimized for both species (Pende & Sogues et al., 2021).

In both organisms, FtsZ was consistently detected as a distinct mid-cell band corresponding to the division site (Figures 7A and 8A), confirming its conserved role in archaeal cytokinesis (Aylett & Duggin, 2017). In dividing cells, FtsZ additionally marked future division planes in daughter cells. In contrast, MinD displayed species-specific localization patterns. In *M. smithii*, MinD signal was broadly distributed throughout the cell and detected at multiple positions along the cell length, without a stable enrichment at mid-cell, sometimes overlapping with FtsZ signal. In *M. kandleri*, MinD was more frequently detected at the division site, often overlapping with the FtsZ signal, particularly in middle and late-stage cells (Figure 8).

Quantitative image analysis supported these qualitative observations. In *M. smithii*, MinD localization appeared spatially dispersed across the cell population, whereas in *M. kandleri*, MinD signals were more centrally enriched and closely aligned with FtsZ localization (Figures 7 and 8 respectively). Notably, in neither organism was MinD excluded from the mid-cell region, in contrast to the pole-restricted localization characteristic of the bacterial MinD system that negatively regulates FtsZ ring formation (Hu & Lutkenhaus, 1999). Together, these results indicate that MinD localization in these methanogenic archaea differs from the canonical bacterial Min system and does not display a pole-restricted pattern under the conditions examined. Neither it seems to be a negative regulator of FtsZ given the sporadic co-localization of FtsZ and MinD in *M. smithii* and the frequent co-localization in *M. kandleri*.

(A)

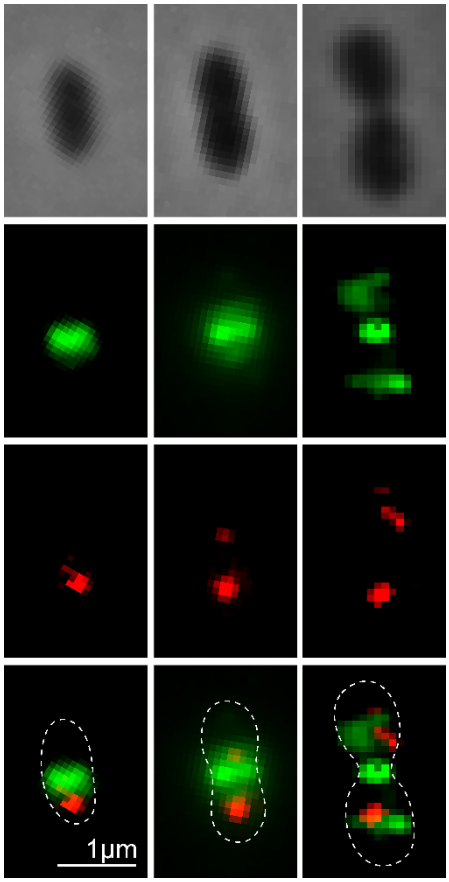

(B)

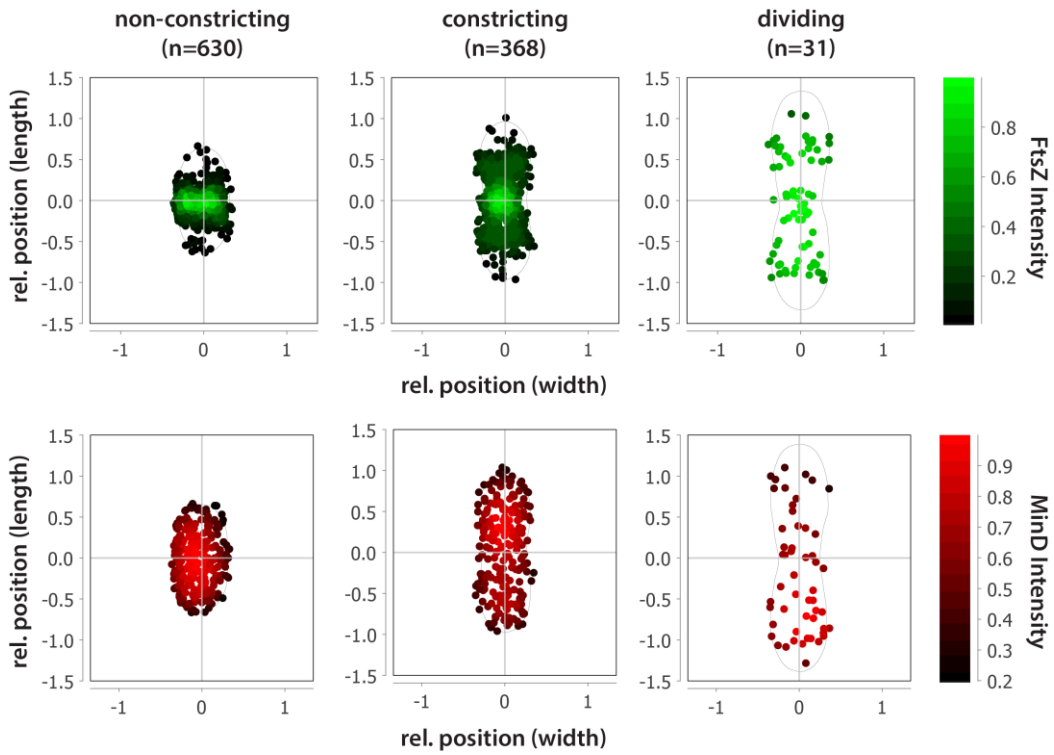

Figure 7: Spatial localization of FtsZ and MinD in *M. smithii* during the cell cycle.

(A) Representative phase-contrast and immunofluorescence images of *M. smithii* cells

showing FtsZ (green) and MinD (red) in non-constricting, constricting, and dividing cells. Cell outlines are indicated by dashed lines; scale bar, 1 µm. (B) shows quantitative localization maps generated by MicrobeJ analysis, depicting the normalized subcellular distribution of FtsZ (green density/intensity maps) and MinD (red density/intensity maps) across the three division stages. Cell numbers analyzed for each category are indicated above the plots.

(A)

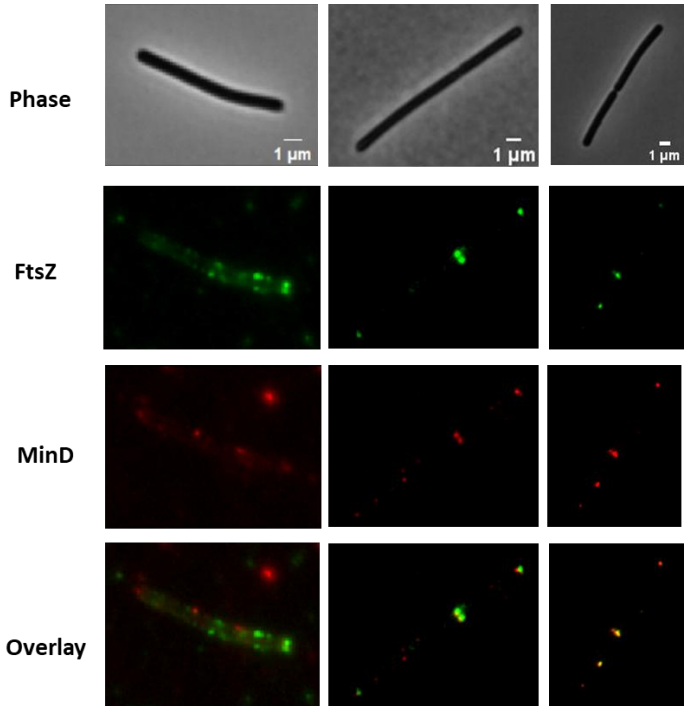

(B)

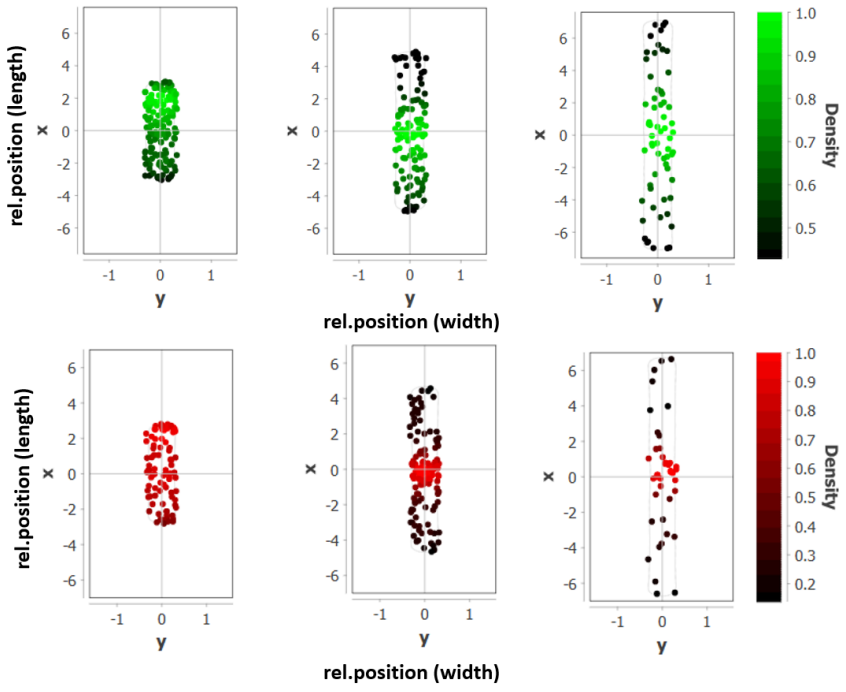

Figure 8: Localization of FtsZ and MinD in *M. kandleri* during the cell cycle.

(A) Representative phase-contrast and immunofluorescence images of *M. kandleri* cells showing FtsZ (green) and MinD (red) localization. Merged images illustrate the relative positioning of MinD with respect to the FtsZ signal; scale bar, 1 µm. (B) shows quantitative MicrobeJ-based analysis of MinD (red) and FtsZ (green) localization, plotted as normalized fluorescence intensity distributions along the cell length and width for small, medium, and large cells. Cell numbers analyzed for each size category are indicated above the plots.

M. smithii and *M. kandleri* contain predominantly one to two MinD foci per cell

Quantification of MinD foci revealed distinct distribution patterns across cell states in the two methanogens (Fig. 9). In *M. smithii*, the majority of cells contained a single MinD focus irrespective of division stage in (Fig. 9A). Non-dividing cells showed the strongest dominance of one focus, whereas constricting cells displayed a modest increase in cells with two foci. Dividing cells exhibited the highest variability, with an increased fraction of cells containing three or four foci, indicating a more dynamic MinD organization during late stages of division.

In *M. kandleri*, a single MinD focus was also the most frequent configuration across all cell-size categories (small, middle, and long) in (Fig. 9B). However, compared to *M. smithii*, *M. kandleri* cells showed greater heterogeneity, particularly in middle and long cells, where two or three foci were more common and occasional cells contained up to five or six foci. Small cells were predominantly characterized by a single focus, whereas increasing cell size correlated with a broader distribution of MinD foci.

Overall, both organisms preferentially exhibit one MinD focus per cell, but *M. smithii* shows tighter control of focus number, while *M. kandleri* displays increased variability with cell size, suggesting species-specific differences in MinD spatial organization and regulation.

(A)

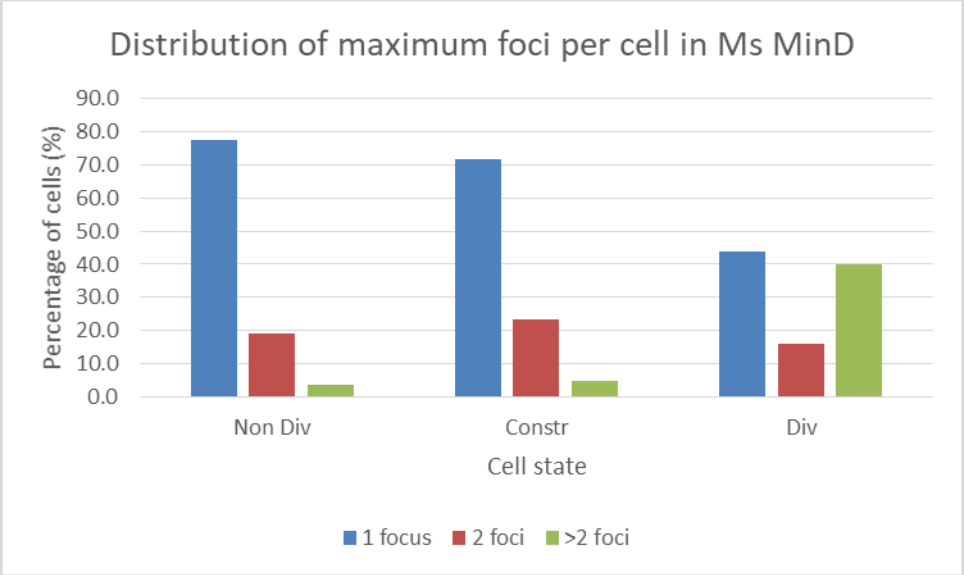

(B)

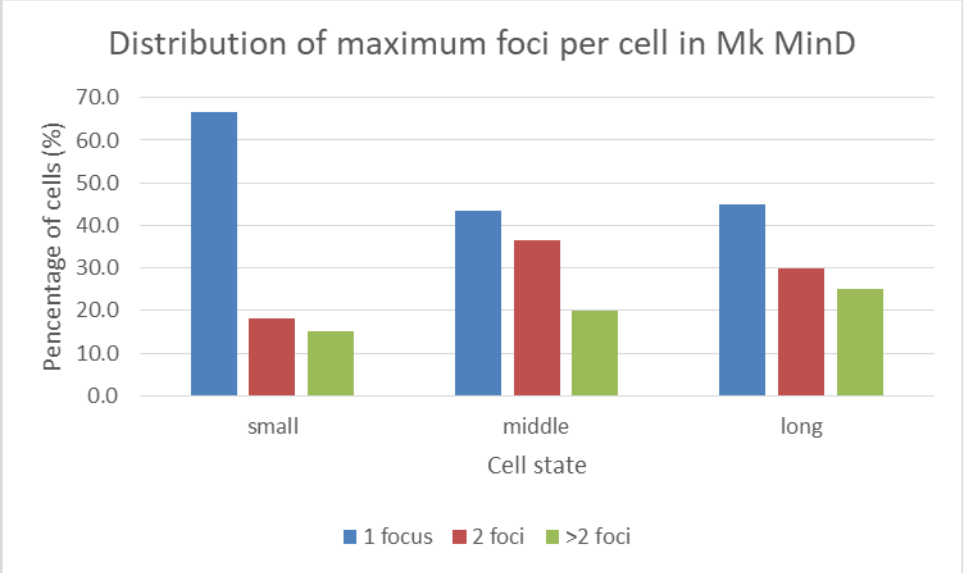

Figure 9: Distribution of MinD foci per cell in *M. smithii* and *M. kandleri*. Bar graphs showing the percentage of cells containing the indicated maximum number of MinD foci. (A) *M. smithii* cells grouped by division stage (non-dividing, constricting, dividing). (B) *M. kandleri* cells grouped by cell-size category (small, middle, long). Colors indicate the number of MinD foci per cell. Quantification was performed from immunolabelled cells using MicrobeJ-based image analysis.

MinD co-localizes with DNA in *M. smithii*

Quantitative image analysis was used to examine MinD localization relative to nucleoid positioning across non-constricting, constricting, and dividing *M. smithii* cells (Fig. 10), using

MicrobeJ-based spatial averaging (Ducret et al., 2016; Pende & Sogues et al., 2021). Across all stages, MinD showed a broad and non-restricted distribution throughout the cell and was not excluded from the midcell region.

When analyzed together with DNA staining, MinD localization exhibited a reproducible spatial relationship with the nucleoid. As the nucleoid reorganized and segregated during cell cycle progression, MinD signal redistributed accordingly and was consistently detected in regions occupied by DNA (Fig. 10). This correlation contrasts with the pole-restricted localization of bacterial MinD and indicates a closer spatial association between MinD and the nucleoid in *M. smithii* (Hu & Lutkenhaus, 1999).

(A)

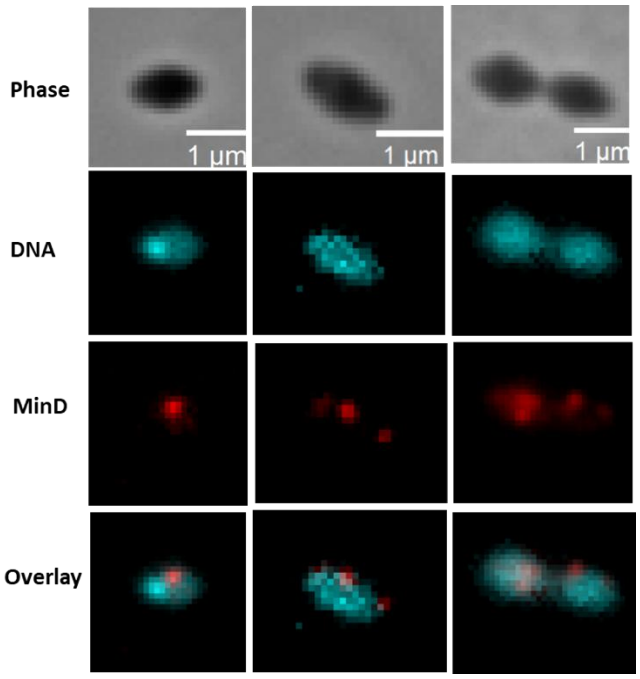

(B)

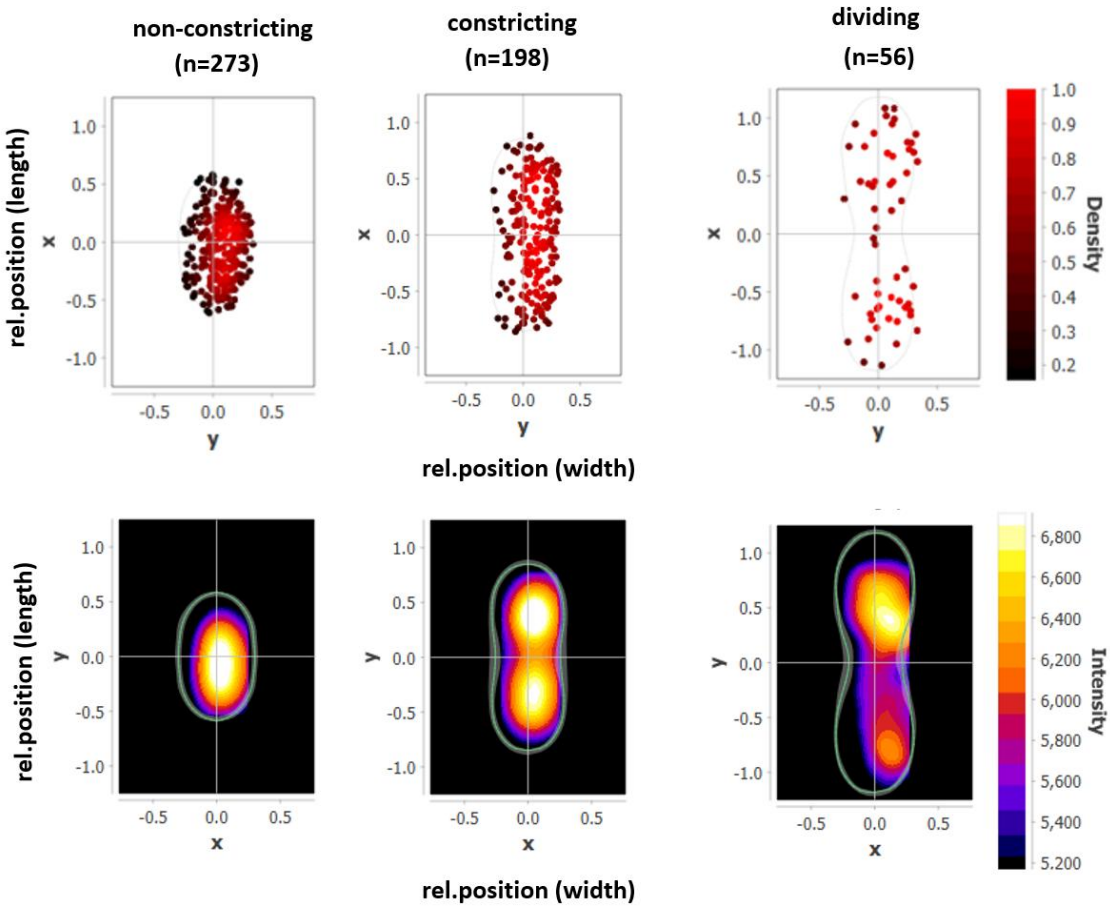

Figure 10: Nucleoid-associated localization of MinD in *M. smithii*.

(A) Representative phase-contrast and fluorescence images of *M. smithii* cells showing DNA stained with Hoechst (cyan) and MinD immunolabelling (red) across non-constricting, constricting, and dividing cells. Merged images illustrate the spatial relationship between MinD foci and the nucleoid, scale bar, 1 µm. (B) shows quantitative MicrobeJ-based image analysis of MinD localization (red density of maximal foci) and DNA distribution (heat maps) plotted relative to normalized cell length and width. Cell numbers analyzed for each division stage are indicated above the plots.

MinD localization between segregating nucleoids in *M. kandleri*

Analysis of MinD and DNA localization in *M. kandleri* revealed a reproducible spatial relationship between MinD foci and segregating nucleoids across the analyzed cell-size categories (small, middle, and large cells; Fig. 11). Cells were categorized by size as a proxy for progression through the cell cycle, and localization patterns were quantified using MicrobeJ-based image analysis (Ducret et al., 2016).

Across all size categories, MinD was detected as one or two discrete foci positioned along the central longitudinal axis of the cell. As cell size increased and the Hoechst-stained nucleoid adopted an elongated and partially segregated configuration, MinD signals were consistently observed in the region between the separating DNA masses rather than overlapping with the bulk of the nucleoid signal. MinD occupied a central position between segregating nucleoids, indicating a spatial association with chromosomal organization rather than with the divisome. Which can be clearly observed from Figure 11.

(A)

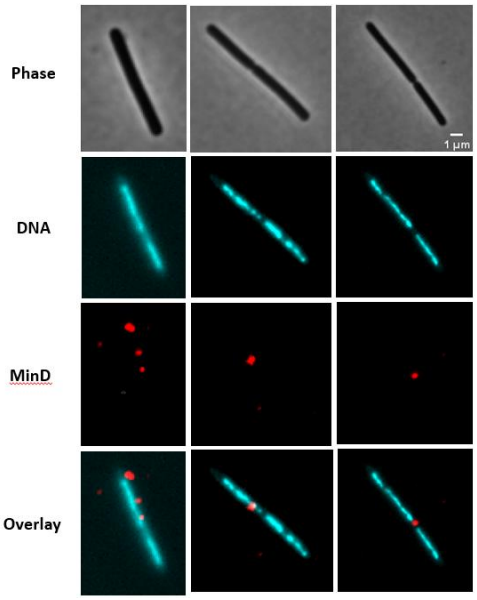

(B)

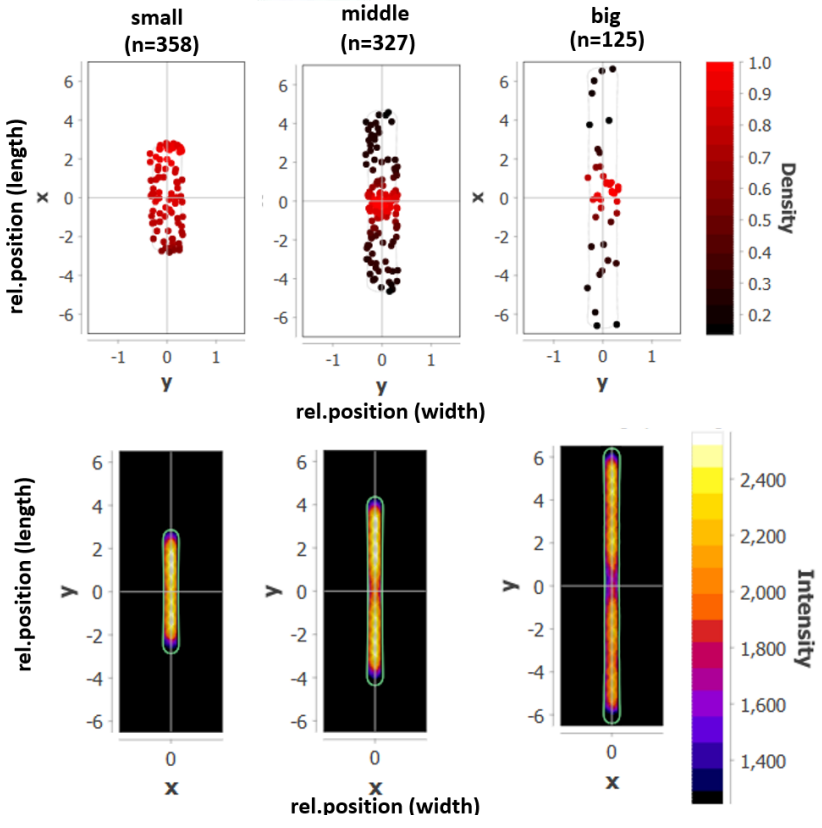

Figure 11: Spatial relationship between MinD and the nucleoid in *M. kandleri*. (A) Representative phase-contrast and fluorescence images of *M. kandleri* cells showing DNA stained with Hoechst (cyan) and MinD immunolabelling (red). Overlay images illustrate the relative positioning of MinD foci with respect to the nucleoid, scale bar, 1 µm. (B) shows quantitative MicrobeJ-based image analysis depicting the distribution of MinD maximal foci (red density plots) and DNA localization (heat maps) along normalized cell length and width for small, medium, and large cells. Cell numbers analyzed for each size category are indicated above the plots.

In silico analysis predicts DNA-binding capacity of MinD from both methanogens

To explore a potential chromosome-associated role of MinD, we first assessed its predicted DNA binding capacity using the Xenusia platform. It is a machine learning based tool trained to identify DNA binding proteins from sequence information and has been validated using diverse bacterial and archaeal protein datasets (Mishra et al., 2021). MinD proteins from *M. smithii* and *M. kandleri* scored among the high-confidence DNA-binding candidates in the Xenusia dataset (Fig. 12), with prediction scores >0.8, placing them within the upper fraction of all analyzed sequences. In contrast, *E. coli* MinD showed a substantially lower DNA binding score, consistent with its established role as a membrane associated ATPase rather than a nucleoid associated protein (Hu & Lutkenhaus, 1999).

These predictions provided an insight for subsequent experimental validation of MinD-DNA interactions using EMSA.

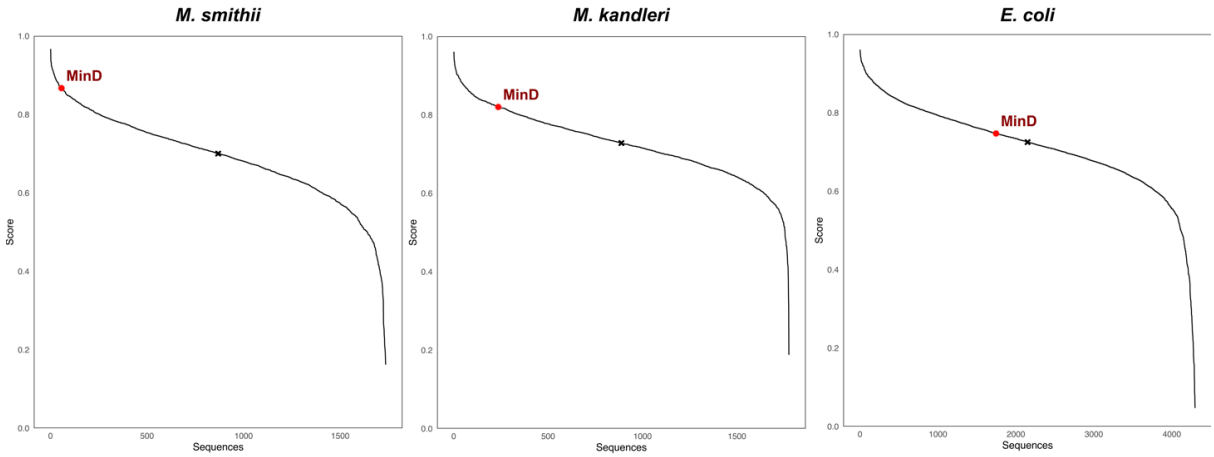

Figure 12: In silico prediction of DNA-binding propensity of MinD using Xenusia performed by Dr. Tobias Viehböck.

Xenusia-based DNA-binding predictions for MinD from *M. smithii* (left), *M. kandleri* (middle) and *E.coli* MinD (right) . Each plot ranks proteins (x-axis) against their predicted DNA-binding score (y-axis; higher values indicate higher likelihood of DNA binding). The position of MinD is highlighted in red. In both species, MinD scores within the higher range of predicted DNA-binding proteins relative to the background proteome, supporting a potential chromosome associated role. The black curve represents the ranked distribution of all analyzed proteins; the marker (x) indicates the median reference position used for comparison. *E. coli* MinD was run as a control and shows no potential DNA-binding property due to the low score.

EMSA analysis shows MinD–DNA binding in both methanogens

To assess the DNA-binding capability of MinD proteins from *M. smithii* and *M. kandleri*, EMSAs were performed with increasing protein concentrations as seen in Figure 13. No shift was observed in the negative controls, including *E. coli* MinD, BSA and heat-inactivated (Hi) protein, indicating the absence of nonspecific binding or artefactual shifts. The DNA/RNA-binding protein Alba, included as a positive control, produced a clear shift, confirming the assay conditions were suitable for detecting protein–DNA interactions.

For *M. smithii* MinD, a slight shift was observed at 50 µmol L^{-1}, which increased modestly at 100 µmol L^{-1}, while a distinct shift was detected at 200 µmol L^{-1}, indicating concentration-dependent binding to DNA. Similarly, *M. kandleri* MinD showed a minor shift at 100 µmol L^{-1} and a clear shift at 200 µmol L^{-1}, demonstrating a comparable concentration-dependent DNA interaction. These results suggest that both archaeal MinD proteins can interact with DNA at higher concentrations, whereas negative controls showed no detectable binding.

Taken together, the results suggest that *M. smithii* and *M.kandleri* MinD are DNA-binding and DNA protein complexes show a MinD concentration-dependent shift.

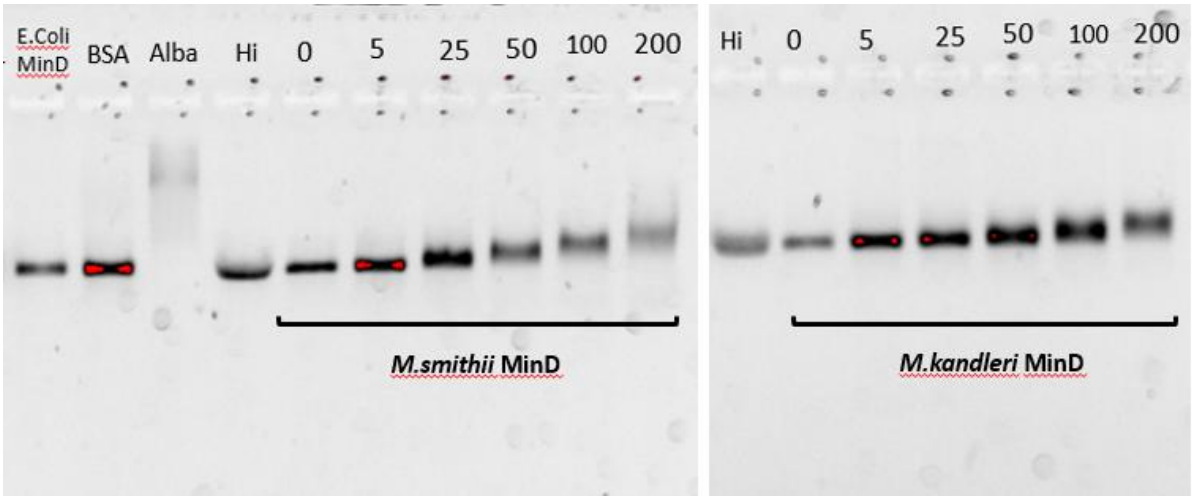

Figure 13: EMSA showing DNA binding by MinD from methanogenic archaea.

EMSA showing concentration-dependent DNA binding by MinD from *M. smithii* (left) and *M. kandleri* (right). For *M. smithii* MinD, lanes show (from left): *E. coli* MinD, BSA (negative control), Alba (positive control), heat-inactivated (HI) *M. smithii* MinD, followed by increasing concentrations of active *M. smithii* MinD (0, 5, 25, 50, 100, 200 µmol L^{-1}). For *M. kandleri* MinD, lanes show heat-inactivated (HI) protein followed by increasing concentrations of active *M. kandleri* MinD (0, 5, 25, 50, 100, 200 µmol L^{-1}).

Co-IP of MinD in *M. kandleri*

Co-IP of MinD from *M. kandleri* followed by mass spectrometry identified a set of proteins significantly enriched in the MinD pulldown compared with the control (Fig. 14). The prepared samples were processed by the Mass Spectrometry facility and downstream proteomic analysis were carried out by Dr. Tobias Viehböck. The analysis was based on biological triplicates, increasing confidence in the identified interaction candidates.

Two complementary analysis strategies were applied: enrichment filtering of proteins detected exclusively in the MinD pulldown, and data imputation to account for missing values, a standard approach in label-free proteomics (Lazar et al., 2016). Both strategies yielded highly consistent results, with the imputed dataset retaining nearly all candidates from the non-imputed analysis. In total, 30 proteins were significantly enriched in the MinD pulldown relative to the control.

MinD itself was the most strongly enriched protein, confirming the specificity of the CoIP. The remaining candidates spanned diverse functional categories, including proteins involved in translation and ribosome function, DNA replication and genome maintenance (e.g. PCNA, ATP-dependent DNA helicase), RNA processing and tRNA modification, central metabolism, methanogenesis, and ABC-type ATPases. Several uncharacterized proteins were also detected. Several of the functional categories are usually found in Co-IPs such as ribosomal proteins and are most likely false positives. More interestingly, a lot of the potential interaction partners were falling in to the category DNA replication/repair/genome maintainace as well as one candidate in RNA-binding/Chromatin/structural proteins (Fig. 14). This functional distribution of enriched proteins indicates that MinD in *M. kandleri* associates with a diverse chromosome associated network. All proteins enriched in the *M. kandleri* MinD Co-IP are listed in the Supplementary Material.

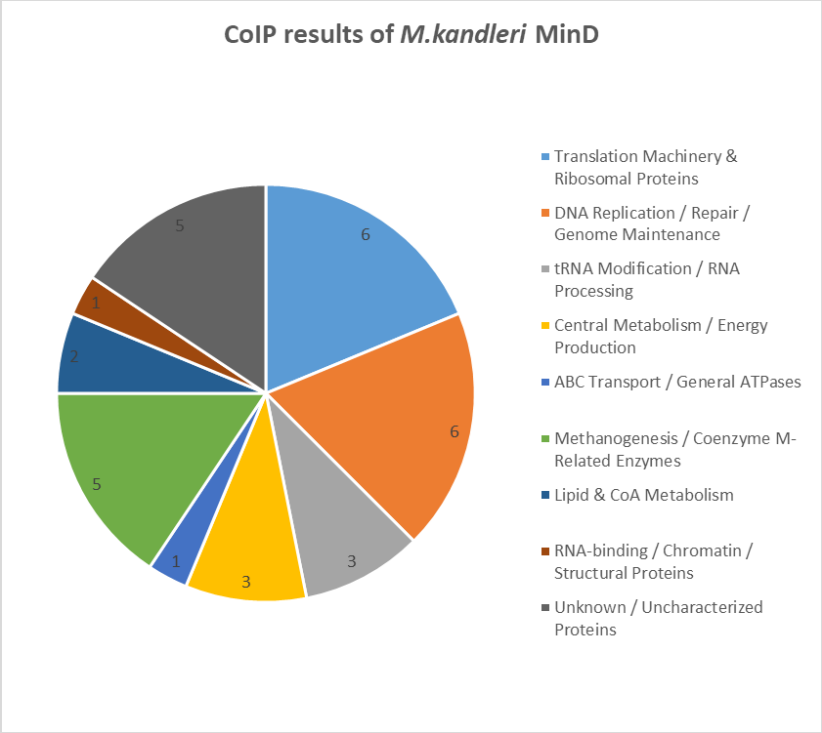

Figure 14: Co-IP analysis of *M. kandleri* MinD

Pie chart summarizing proteins significantly enriched in the MinD pulldown relative to the control, based on mass spectrometry analysis of biological triplicates. Identified interaction partners are grouped by functional category, including translation machinery and ribosomal proteins, DNA replication and repair, RNA processing, methanogenesis-related enzymes, ATPases, lipid and CoA metabolism, chromatin-associated proteins and uncharacterized proteins. Numbers indicate the count of proteins within each functional category.

Co-IP of MinD in *M. smithii*

Co-IP of MinD from *M. smithii* followed by mass spectrometry identified MinD as the most strongly enriched protein, together with seven additional statistically significant interaction partners (Fig. 15), confirming successful and specific pulldown of the bait protein. The enriched proteins belonged to diverse functional categories, including nucleotide-binding ATPases, DNA and chromosome metabolism, protein folding and chaperone activity, translation-associated factors, DNA/RNA-binding regulatory proteins and metabolic enzymes. The *M. smithii* dataset contained fewer interaction partners compared to *M. kandleri*, likely reflecting reduced statistical power, as the *M. smithii* Co-IP was performed in technical duplicates only.

Notably, none of the proteins identified in the *M. smithii* MinD CoIP overlapped with homologous protein groups detected in the *M. kandleri* MinD CoIP, indicating distinct, species-specific MinD interaction profiles. However, like in *M. kandleri* some interaction partners included proteins belonging to the DNA/chromosome metabolism and DNA/RNA binding/regulatory category. Pointing to the possible involvement of MinD from *M. smithii* and *M. kandleri* in chromosome biology. All proteins enriched in the *M. smithii* MinD Co-IP are listed in the Supplementary Material.

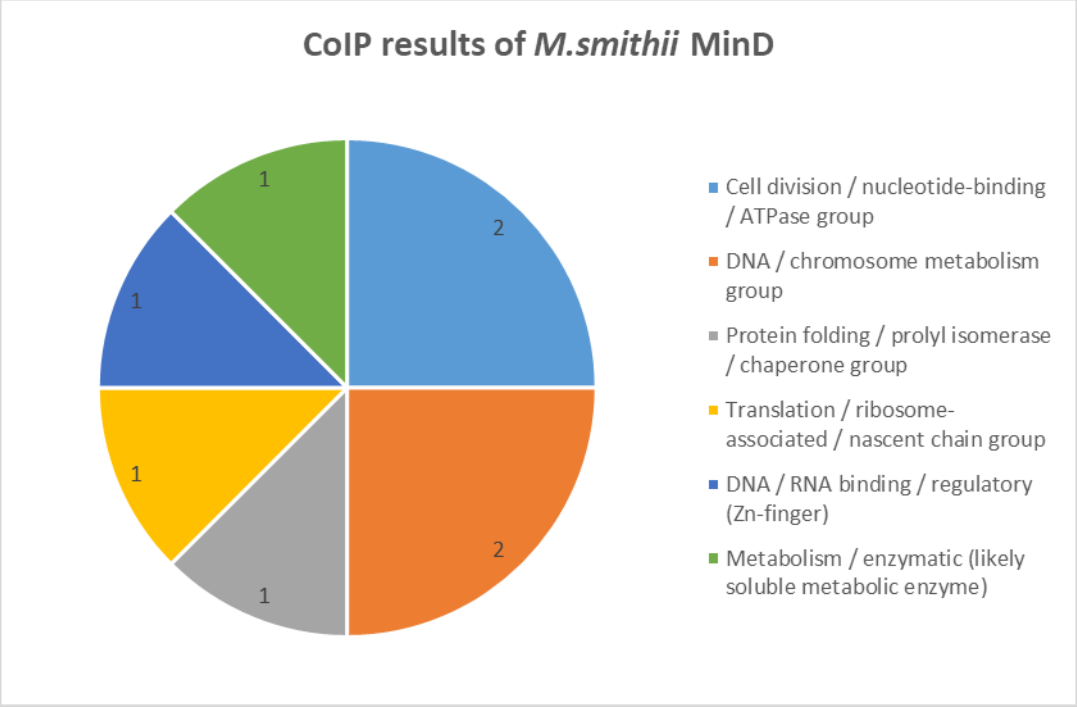

Figure 15: Co-IP analysis of *M. smithii* MinD interaction partners.

Pie chart summarizing proteins identified by MinD Co-IP and mass spectrometry in *M.*

smithii. Identified hits are grouped by predicted functional categories, including cell division/nucleotide-binding ATPases, DNA/chromosome metabolism, protein folding and chaperone functions, translation-associated proteins, DNA/RNA-binding regulatory proteins, and metabolic enzymes. Numbers within each sector indicate the number of significant hits per functional category. MinD was the most strongly enriched protein, confirming successful and specific pulldown of the bait.

Discussion Part 1

ATPase activity of MinD in methanogenic archaea

The ATPase assay demonstrates that MinD from both *M. smithii* and *M. kandleri* is an active P-loop NTPase, as ATP-dependent phosphate release was observed exclusively in reactions containing MinD and ATP, but not in any control conditions. This confirms that ATP hydrolysis is an intrinsic property of methanogenic MinD, consistent with the conserved Walker A and Walker B motifs identified in sequence analyses and with the biochemical behavior of MinD- and ParA-family ATPases more broadly (Hu & Lutkenhaus, 1999; Leonard et al., 2005). Under identical assay conditions, *M. smithii* MinD exhibited higher apparent ATPase activity than *M. kandleri* MinD. This difference is likely influenced by assay temperature, as *M. kandleri* is a hyperthermophile with an optimal growth temperature close to 98 °C, and ATPase activity of thermophilic proteins is often underestimated at room temperature (Vieille & Zeikus, 2001; Slesarev et al., 2002). Increasing the assay temperature may therefore reveal higher catalytic activity for *M. kandleri* MinD. Overall, these results establish MinD as a functional ATPase in both methanogens, providing a biochemical basis for its proposed ParA-like behavior and supporting subsequent analyses of DNA binding and intracellular localization.

Western blot analysis of MinD and FtsZ

Western blot analysis confirmed the specificity of antibodies against MinD and FtsZ using purified recombinant proteins, which migrated at the expected molecular weights reported for archaeal homologs (Pende & Sogues et al., 2021; Nußbaum et al., 2020; Nußbaum et al., 2021). Detection of these proteins in whole-cell lysates required inclusion of protease inhibitor tablets during lysis, indicating substantial proteolytic activity in methanogenic archaea. This is

consistent with the biochemical fragility of archaeal proteins during extraction and highlights the need for stringent protease inhibition (Albers & Meyer, 2011).

Efficient cell disruption was achieved by bead beating, which is necessary to break the robust archaeal cell envelope composed of archaeal PG and associated protein layers (Albers & Meyer, 2011; van Wolferen et al., 2022). Following optimization, MinD and FtsZ were readily detected in *M. smithii* and in *M. kandleri* lysates.

Overall, these results validate antibody specificity and confirm expression of key division proteins, while underscoring technical limitations inherent to Western blot analysis of archaeal cell extracts.

Optimization of immunolabelling and species-specific MinD localization

Immunolabelling of methanogenic archaea required substantial optimization due to the structural rigidity of archaeal PG. In *M. smithii*, efficient permeabilization depended on the use of PeiW, an archaeal PG specific endoisopeptidase previously shown to enable antibody access in this organism (Pende & Sogues et al., 2021). Given that *M. smithii* and *M. kandleri* both have a PG cell wall, PeiW was also used in *M. kandleri*, albeit in higher concentration. Fine-tuning of PeiW concentration and methanol fixation conditions was essential to balance antibody penetration with preservation of cellular integrity. Similar challenges have been reported for immunolabelling of MinD, where fixation and permeabilization critically influence detection of MinD and ParA family ATPases (Hu & Lutkenhaus, 1999; Vecchiarelli et al., 2014).

Quantitative image analysis revealed striking species-specific differences in MinD localization. In *M. smithii*, MinD displayed a broad intracellular distribution that correlated with nucleoid reorganization during the cell cycle, resembling the behavior of ParA-like ATPases involved in chromosome organization and segregation, as described in bacteria such as *Caulobacter crescentus* (Mohl & Gober, 1997).

In contrast, in *M. kandleri*, MinD showed pronounced colocalization with FtsZ at the septation plane. This localization is fundamentally distinct from the canonical Min system in *E. coli*, where MinD oscillates between the poles and is excluded from midcell to negatively regulate FtsZ assembly (Hu & Lutkenhaus, 1999). The midcell association of MinD in *M. kandleri*

therefore represents a non-canonical, archaeal-specific MinD behavior that is not consistent with classical bacterial MinD function.

Together, these observations indicate that MinD has diverged functionally between methanogenic species. Rather than serving a single conserved role, archaeal MinD appears to have been adapted to distinct cellular functions, ranging from chromosome-associated processes to division-site-linked localization, underscoring the evolutionary flexibility of ParA/MinD-family ATPases.

DNA-binding properties of MinD revealed by EMSA

Electrophoretic mobility shift assays demonstrated that MinD from *M. smithii* and *M. kandleri* is capable of interacting with DNA in vitro, although detectable shifts were observed only at high protein concentrations. This concentration dependence suggests a weak or transient interaction rather than high-affinity, sequence-specific DNA binding. The specificity of this interaction was supported by appropriate controls: heat-inactivated MinD failed to shift DNA, the non–DNA-binding protein BSA showed no interaction and *E. coli* MinD did not produce a shift under identical conditions. In contrast, the chromatin-associated protein Alba generated a strong mobility shift, confirming the validity of the assay conditions.

Low-affinity, non-sequence-specific DNA binding is a hallmark of ParA family ATPases, which interact dynamically with the nucleoid to generate spatial gradients or to organize intracellular cargos rather than forming stable DNA–protein complexes (Vecchiarelli et al., 2014; Schumacher, M.A. 2012). Similar weak DNA-binding behavior has been reported for bacterial ParA proteins involved in chromosome and plasmid segregation (Hatano & Niki, 2010; Leonard et al., 2005). The EMSA results therefore support the idea that archaeal MinD retains ParA-like biochemical properties, consistent with phylogenetic analyses placing archaeal MinD as a separate group from the canonical bacterial MinD and within the ParA-like ATPase superfamily (Pulianmackal & Vecchiarelli, 2024, Nußbaum et al., 2020).

Taken together, these findings provide biochemical evidence that MinD from both methanogens can associate with DNA, but the weak nature of the interaction suggests a regulatory or organizational role rather than direct sequence-specific binding. EMSA alone cannot resolve whether this interaction contributes to chromosome segregation, nucleoid

organization, or condensation in vivo, emphasizing the importance of integrating these results with localization and Co-IP analyses.

MinD Co-IP Results in Methanogens

Co-IP coupled to mass spectrometry reveals that MinD participates in distinct and species-specific interaction networks in *M. kandleri* and *M. smithii*. In *M. kandleri*, MinD was enriched with a broad spectrum of proteins, including chromatin-associated factors (notably Alba), DNA replication and maintenance proteins such as PCNA and ATP-dependent DNA helicases, as well as components of translation and methanogenesis. The robustness of this dataset, derived from biological triplicates, supports a genuine association of MinD with chromosome-related processes rather than nonspecific background interactions.

The enrichment of Alba is particularly informative. Alba is a major archaeal chromatin protein involved in DNA binding, chromatin organization, and genome stability (Takemata & Bell, 2021). Its association with MinD aligns with the ParA-like evolutionary placement of archaeal MinD proteins (Pulianmackal & Vecchiarelli, 2024) and is consistent with the DNA-binding activity observed in EMSA experiments. Similarly, the co-enrichment of PCNA and helicases suggests a potential spatial or functional coupling of MinD to replication-associated chromosomal regions, a feature previously described for ParA-family ATPases that organize DNA or DNA-bound cargos rather than acting as site-specific transcription factors (Vecchiarelli et al., 2014; Leonard et al., 2005).

In *M. smithii*, MinD Co-IP yielded fewer significant interaction partners, likely reflecting the lower experimental depth (biological duplicates). Nevertheless, the identification of DNA topoisomerase is notable, as topoisomerases play central roles in resolving DNA topology during replication and segregation, further supporting a chromosome-associated context for MinD activity. Importantly, no homologous interaction partners were shared between *M. smithii* and *M. kandleri*, indicating that MinD interaction networks are not conserved at the level of specific binding partners, but rather reflect organism-specific integration into cellular pathways.

Together, the Co-IP data support a model in which MinD functions as a flexible ParA-like ATPase module in methanogens, capable of associating with chromatin and genome maintenance machineries in a species-dependent manner. Rather than acting as a conserved

divisome-positioning factor analogous to bacterial MinD, methanogen MinD appears to participate in broader chromosome-associated processes, consistent with its phylogenetic placement and biochemical properties. These findings identify chromatin proteins such as Alba and replication factors such as PCNA as key candidates for future mechanistic studies aimed at defining MinD function in archaeal chromosome biology.

Results Part 2: Function of SepF in *M. kandleri*

SepF Western Blot of *M. kandleri* whole cell lysate and purified protein

Despite repeated optimization of Western blot conditions, including variation of lysis parameters and the inclusion of protease inhibitor cocktails, SepF could not be detected in *M. kandleri* whole-cell lysates by Western blot, despite clear detection of the purified protein (Fig. 16).

However, based on previous whole proteome analysis of *M. kandleri*, SepF is expressed in exponentially growing *M. kandleri* cells (personal communication with Dr. Nika Pende). Even if we weren't unable to see expression on Westernblot, we decided to proceed with immunolabelling of *M. kandleri* cells as well as Co-IP.

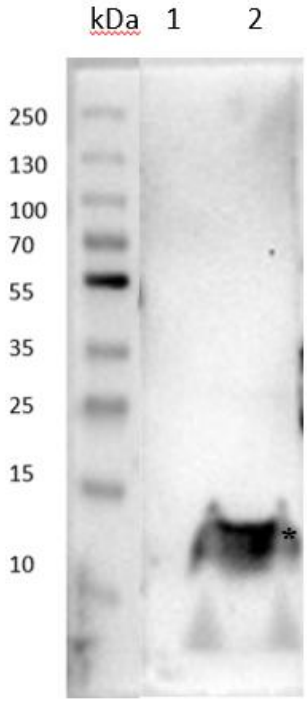

Figure 16: Western blot analysis of SepF in *M. kandleri* (Mk). (*) indicates the protein band corresponding to the expected size. Lanes 1–2: *M. kandleri* cell lysate and purified SepF (primary anti-SepF, 1:500; secondary anti-rat, 1:1000)

SepF co-localizes with FtsZ at division site in *M. kandleri*

Immunolabelling of *M. kandleri* required several organism-specific adaptations relative to protocols established for *M. smithii*. Due to the formation of soft and poorly compacting cell pellets, centrifugation steps were performed for extended durations to ensure sufficient cell recovery during washing and staining. In addition, a larger culture volume was processed per sample (4 mL of early exponential-phase culture for *M. kandleri*, compared with 2 mL typically used for *M. smithii*) to obtain adequate cell material for reliable immunofluorescence analysis. These adjustments were necessary to compensate for differences in cell morphology and sedimentation behavior between the two methanogens.

Fluorophore selection was optimized to minimize spectral bleed-through between channels. SepF was detected using an anti-rat secondary antibody, and fluorophores with well-separated excitation and emission spectra were chosen, most commonly Alexa Fluor 488 and Alexa Fluor 647. Closely overlapping fluorophore combinations, such as Alexa Fluor 488 and Alexa Fluor 555, were avoided to reduce channel cross-talk and improve signal discrimination. Similar strategies have been recommended for multicolor fluorescence imaging to ensure accurate localization analysis (Lichtman & Conchello, 2005; Pende & Sogues et al., 2021).

All other steps of the immunolabelling procedure, including permeabilization, fixation, antibody incubation, and washing conditions, were performed as described for methanogenic archaea with minor optimization (Pende & Sogues et al., 2021). Using these adjusted conditions, reproducible detection of SepF and FtsZ signals was achieved in *M. kandleri*, enabling subsequent qualitative and quantitative image analysis.

Immunolablling of *M. kandleri* revealed a clear SepF signal concentrated at the midcell, coincident with the position of the FtsZ division ring (Fig. 17A). Overlay images showed substantial spatial overlap between SepF and FtsZ, indicating that SepF colocalizes with the cytokinetic ring in *M. kandleri*. Quantitative image analysis (Fig. 17B), in which fluorescence maxima were plotted relative to normalized cell length and width, further confirmed this observation. Across all three analysed cell-cycle stages (small, intermediate, and dividing cells), SepF consistently localized to the septation plane together with FtsZ, demonstrating that SepF recruitment to the division site is a robust and stage-independent feature in *M. kandleri*.

This localization pattern closely mirrors previous findings in *M. smithii*, where SepF was shown to function as the primary membrane anchor and spatial organizer of FtsZ (Pende et al., 2021). Similar SepF–FtsZ colocalization has also been reported in other archaeal systems, including *H. volcanii*, where SepF interacts with FtsZ paralogues and contributes to proper Z-ring architecture and stability (Nußbaum et al., 2021; Nußbaum et al., 2023). Together, these observations strongly support the conclusion that SepF acts as a conserved FtsZ-associated divisome component in *M. kandleri*. Despite the presence of an additional bacterial-type anchor, FtsA, in *M. kandleri*, the consistent midcell localization of SepF alongside FtsZ suggests that SepF plays a central role in anchoring and organizing the FtsZ ring in this organism, analogous to its function in other archaeal and selected bacterial lineages.

(A)

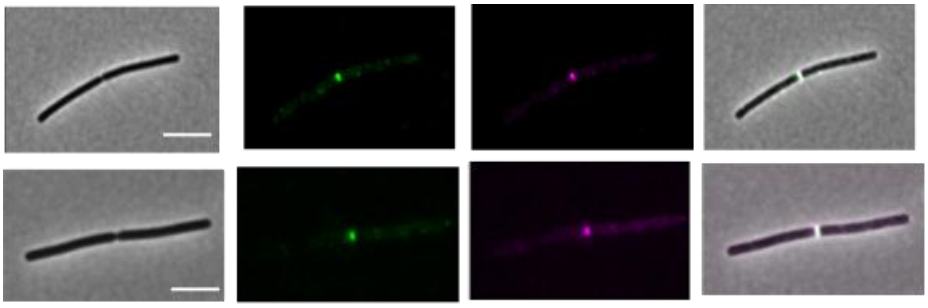

(B)

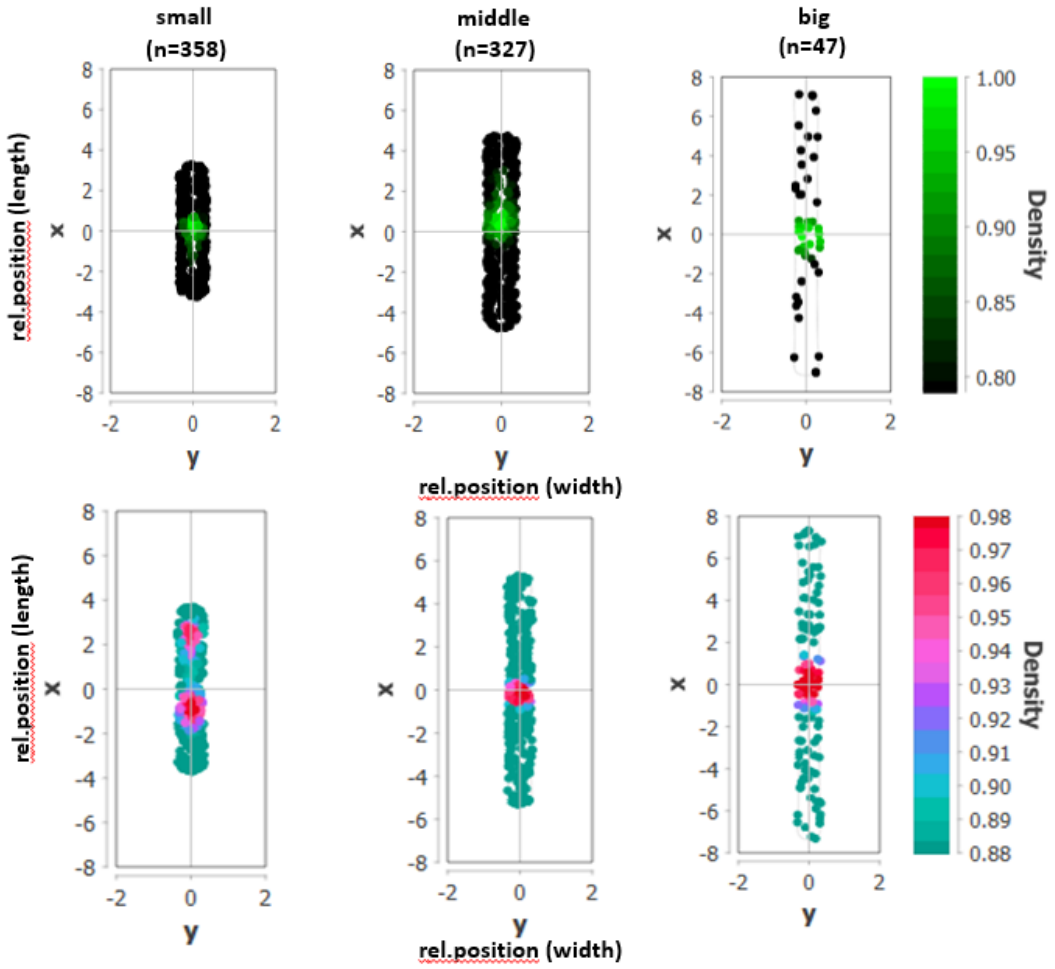

Figure 17: Immunolabelling and quantitative image analysis of FtsZ and SepF in *M. kandleri*.

(A) Representative phase-contrast and fluorescence microscopy images showing FtsZ (green) and SepF (magenta) localization in *M. kandleri* cells . Overlay images illustrate co-localization of FtsZ and SepF at the division site. Scale bars, 1 µm. (B) Quantitative image analysis was performed using MicrobeJ and displays normalized subcellular localization patterns of FtsZ (top row) and SepF (bottom row) across cells grouped by size (small, middle, big). Density and intensity maps indicate enrichment of both proteins at midcell, consistent with their role in divisome organization.

Co-IP of SepF in *M. kandleri*

Co-IP of SepF from *M. kandleri* followed by mass spectrometry identified SepF as the most strongly enriched protein ($log_2FC \approx 6$), confirming antibody specificity and successful pulldown. The prepared samples were processed by the Mass Spectrometry facility and statistical evaluation were carried out by Dr. Tobias Viehböck. Due to the absence of biological

triplicates, interpretation was restricted to proteins enriched in the SepF fraction ($log_2FC > 1$) or detected exclusively in the SepF pulldown (Fig. 18).

Among the enriched proteins were core cell division factors, including FtsZ and MinD, consistent with the established role of SepF as an FtsZ-binding and membrane-anchoring protein in archaea (Duggin et al., 2015; Pende & Sogues et al., 2021). In addition, several proteins involved in chromosome replication and genome maintenance, such as PCNA**,** DNA topoisomerase I, and reverse gyrase, were recovered, suggesting spatial proximity between SepF and chromosomal processes during the cell cycle (Kelman & White, 2005; Grogan, 2015). The dataset also included RNA- and DNA-binding proteins, including Alba-related and regulatory factors, indicating potential coupling between divisome assembly and nucleoid-associated functions. All proteins enriched in the *M. kandleri* SepF Co-IP are listed in the Supplementary Material.

Overall, despite limited replication, the SepF Co-IP results support a model in which SepF in *M. kandleri* associates with both cytokinetic and chromosome associated protein networks, consistent with an integrated organization of cell division and genome maintenance in archaea.

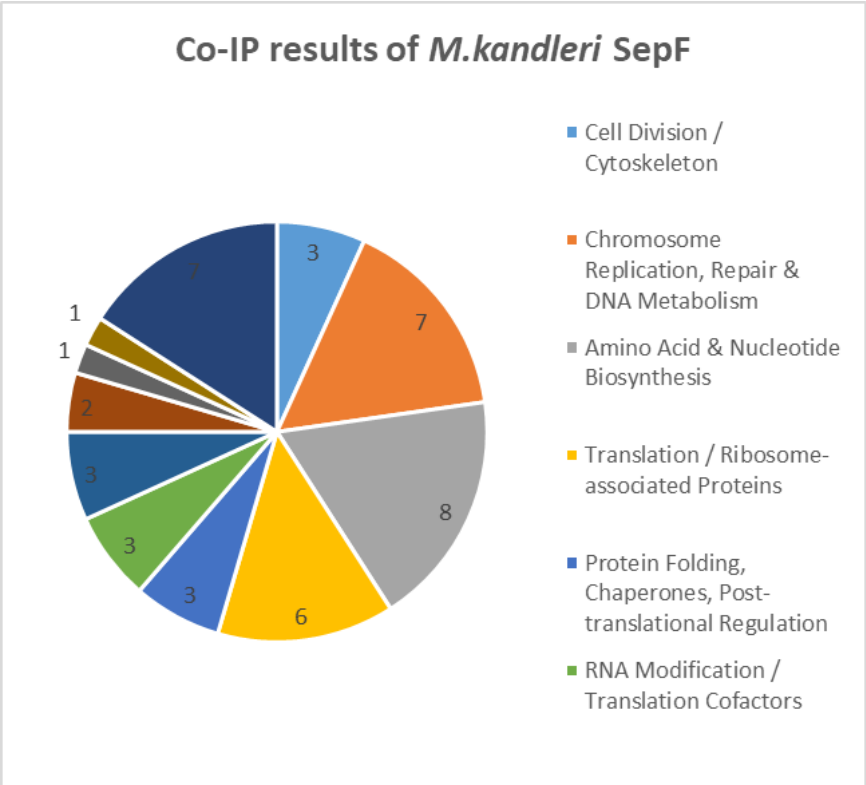

Figure 18: Functional classification of proteins co-immunoprecipitated with SepF in *M. kandleri*.

Pie chart summarizing the distribution of proteins identified by SepF Co-IP followed by mass spectrometry. Proteins are grouped according to predicted functional categories, including cell division/cytoskeleton, chromosome replication and DNA metabolism, translation and ribosome-associated proteins, protein

Discussion Part 2

Western blot, immunolabelling, and image analysis of SepF in M. kandleri

Despite repeated optimization of Western blot conditions, including the use of protease inhibitor cocktails, SepF could not be detected in whole-cell lysates of *M. kandleri*. This likely reflects a combination of poor solubility under denaturing conditions or epitope masking during sample preparation which might be limitations that have been reported previously for archaeal cytoskeletal proteins, particularly in hyperthermophiles (Bernander & Ettema et al.,, 2010; Aylett & Duggin, 2017). Importantly, the absence of a detectable SepF signal by Western blot does not indicate lack of expression.

Independent experimental approaches clearly demonstrate the presence and cellular relevance of SepF in *M. kandleri*. Immunolabelling using anti-SepF antibodies consistently revealed distinct intracellular SepF signals, which colocalized with FtsZ at the septation plane across all analyzed cell-cycle stages. This spatial pattern is consistent with the established role of SepF as an FtsZ-binding protein and membrane anchor in both bacteria and archaea (Duman et al., 2013; Nußbaum et al., 2021; Nußbaum et al., 2023). Quantitative image analysis further confirmed that SepF localization is maintained from early constriction through division, supporting its role as a stable component of the archaeal divisome.

The presence of SepF was further validated by Co-IP followed by mass spectrometry, where SepF was the most strongly enriched protein. The co-enrichment of FtsZ and MinD among SepF interaction partners supports the conclusion that SepF participates in a functional divisome complex in *M. kandleri*, consistent with its established role as an FtsZ-binding membrane anchor in bacteria and other archaea (Duman et al., 2013; Pende & Sogues et al., 2021; Nußbaum et al., 2021).

Together, these results indicate that SepF is a *bona fide*, functionally relevant divisome protein in *M. kandleri*, despite being refractory to detection by conventional Western blotting. This

underscores the importance of combining immunolabelling, image analysis and proteomics to accurately characterize cytoskeletal proteins in archaeal systems.

SepF interaction network in M. kandleri

Co-IP of SepF in *M. kandleri* identified SepF as the most strongly enriched protein ($log_2FC \sim 6$), confirming antibody specificity, successful pulldown and expression of SepF in *M. kandleri* cells. The enrichment of FtsZ and MinD supports a conserved role for SepF as a core divisome component, consistent with its established function as an FtsZ-interacting membrane anchor in bacteria and archaea (Duman et al., 2013; Nußbaum et al., 2021).

In addition to divisome proteins, SepF co-purified with factors involved in chromosome replication and maintenance, including PCNA, DNA topoisomerase I, reverse gyrase and RecB-like nucleases. Similar associations between division proteins and genome maintenance factors have been reported in archaea, where cytokinesis is closely coordinated with chromosome replication and segregation (van Wolferen et al., 2022; Aylett & Duggin, 2017).

Translation-related and metabolic proteins were also detected, likely reflecting indirect or context-dependent associations common in archaeal Co-IP datasets. As the analysis was performed in technical duplicates, the most biologically relevant candidates are those strongly enriched in the SepF pulldown. Overall, these data support a model in which SepF in *M. kandleri* functions as a central divisome protein that potentially interfaces with chromosome-associated processes, rather than acting solely as a structural FtsZ anchor.

Conclusion

In this study, the archaeal MinD homologs from *M. smithii* and *M. kandleri* were investigated to clarify their biochemical activity, localization and potential cellular function. Phylogenetic analyses place methanogenic MinD within the ParA/MinD family of deviant Walker-type ATPases and biochemical assays confirmed that MinD from both organisms exhibits ATPase activity, consistent with this classification.

Immunolabelling and quantitative image analysis demonstrate that MinD does not function as a negative regulator of FtsZ in either species, unlike the bacterial Min system. In *M. smithii*, MinD is broadly distributed throughout the cell but shows a reproducible spatial relationship with the nucleoid, with MinD redistribution accompanying DNA segregation during the cell

cycle. In *M. kandleri*, MinD frequently localizes between segregating nucleoids and does not display a stable association with the FtsZ division site, indicating that its role is distinct from divisome positioning.

Both in silico predictions and in vitro EMSA experiments support the ability of MinD to bind DNA, albeit with low affinity, a characteristic feature of ParA-like ATPases. Co-IP further revealed that MinD interacts with multiple DNA, RNA and chromatin associated proteins in both methanogens, strengthening the link between MinD and chromosome associated processes.

Overall, the combined data indicate that MinD in methanogenic archaea is unlikely to function as a bacterial-like regulator of Z-ring placement. Instead, MinD appears to be a ParA-like ATPase with a role linked to chromosome biology, potentially contributing to nucleoid organization or segregation. These findings highlight the functional diversity of archaeal MinD proteins and underscore the evolutionary flexibility of cell cycle regulation mechanisms in Archaea.

In parallel, SepF was established as a *bona fide* divisome component in *M. kandleri*. SepF colocalizes with FtsZ throughout the cell cycle and was strongly enriched in Co-IP experiments, supporting its conserved role as an FtsZ-associated membrane anchor in archaeal cytokinesis.

Outlook and Future Directions

This study establishes that MinD from methanogenic archaea is a ParA-like ATPase with ATPase activity and DNA-binding capacity, yet its precise cellular function remains unresolved. While immunolabelling, EMSA, and Co-IP data clearly demonstrate an association of MinD with chromosomal DNA and DNA/RNA-associated proteins, the current dataset cannot distinguish whether MinD plays a direct role in chromosome segregation or instead functions more broadly in chromosome positioning, scaffolding, or nucleoid organization. Both interpretations are compatible with the observed low-affinity DNA binding, dynamic intracellular localization, and interaction with chromatin associated proteins.

In Archaea, chromosome segregation and organization are known to rely on multiple systems. Several archaeal lineages encode SegA/SegB, functional homologs of the bacterial ParABS

system, which mediate origin positioning and chromosome segregation in species such as *Sulfolobus* and *Thermococcus* (Robinson et al., 2007; Schumacher et al., 2015). In parallel, SMC-family proteins play a central role in large-scale chromosome organization and compaction across Archaea, including methanogens (Cobbe & Heck, 2004; Hirano, 2016). Comparative genomic analyses indicate that MinD frequently co-occurs with SegAB and/or SMC systems but is not universally conserved across FtsZ-containing archaea, suggesting that MinD may act as an auxiliary or lineage-specific chromosome-associated ATPase, rather than as a core segregation motor (Ithurbide et al., 2022).

Discriminating between these possible roles will require functional genetic perturbation, which is currently not feasible in *M. smithii* and *M. kandleri* due to limited genetic tools. A key future direction is therefore the transfer of these questions into genetically tractable methanogenic model systems, such as *Methanothermobacter marburgensis* or *Methanobacterium thermoautotrophicum*, where targeted gene deletion or depletion strategies are established (Thauer et al., 2008; Fink et al., 2021). Combining *minD* knockouts or ATPase-dead mutants with fluorescence microscopy of DNA, SegAB components, and SMC proteins would allow direct testing of MinD's contribution to chromosome segregation versus higher-order nucleoid organization.

More broadly, this work highlights the need to expand archaeal cell biology beyond a small set of classical model organisms. The diversity of chromosome segregation strategies revealed by comparative genomics—ranging from SegAB-based systems to SMC-dominated architectures suggests that MinD has been evolutionarily repurposed in different archaeal lineages (Bernander & Lindås, 2014; Ithurbide et al., 2022). Future studies integrating genetics, live-cell imaging, and biochemistry across multiple archaeal models will be essential to define how ParA/MinD-like ATPases contribute to chromosome biology in Archaea.

Supplementary tables

Table 1: Proteins enriched in the MinD Co-IP of *M. kandleri*, ranked by $\log_2$ fold change and grouped by functional category

Rank	$\log_2$FC	Protein	Functional category
1	8.16	**MinD (archaeal)**	Cell division / MinD-related (bait)

Rank	log_2FC	Protein	Functional category
2	5.42	Probable tRNA pseudouridine synthase B	tRNA modification / RNA processing
3	4.95	DNA-binding transcriptional repressor of phenylacetic acid degradation	DNA / RNA binding & regulation
4	3.62	Metallophosphoesterase (RNA repair / RNA ligase-activating)	DNA/RNA metabolism
5	3.22	Pyruvate carboxylase [Energy production and conversion]	Central metabolism / energy production
6	2.76	Elongation factor 1-alpha (EF-1α)	Translation machinery
7	2.61	Predicted ATPase of the ABC class	General ATPases
8	2.46	Uncharacterized conserved protein (DUF169 family)	Unknown / uncharacterized
9	2.34	Methyl-coenzyme M reductase II (MCRII)	Methanogenesis
10	2.26	Methyl-coenzyme M reductase, alpha subunit	Methanogenesis
11	2.23	Tetrahydromethanopterin S-methyltransferase	Methanogenesis
12	2.09	DNA/RNA-binding protein Alba (hit 1)	Chromatin / nucleoid organization
13	1.87	Succinyl-CoA synthetase, beta subunit	Energy metabolism
14	1.72	PccA; acetyl/propionyl-CoA carboxylase (α)	Lipid & CoA metabolism
15	1.70	Methanogenesis marker protein 3 (UPF0288 family)	Methanogenesis
16	1.70	ATP-dependent DNA helicase	DNA replication / repair
17	1.66	Archaeosine tRNA-guanine transglycosylase	tRNA modification
18	1.60	DNA/RNA-binding protein Alba (hit 2)	Chromatin / nucleoid organization
19	1.54	DUF3138 protein	Unknown / uncharacterized
20	1.47	Small ribosomal subunit protein eS1	Translation / ribosome
21	1.40	Large ribosomal subunit protein L18E	Translation / ribosome
22	1.38	Ribosomal protein S17E	Translation / ribosome

Rank	log_2FC	Protein	Functional category
23	1.33	PDCD5 / TFAR19-related DNA-binding protein	DNA / RNA binding
24	1.33	Putative methanogenesis marker protein 7	Methanogenesis
25	1.31	tRNA-splicing endonuclease EndA	RNA processing
26	1.28	Hypothetical protein TM0021	Unknown / uncharacterized
27	1.16	Eukaryotic translation initiation factor 2γ (eIF2γ)	Translation initiation
28	1.08	Methyl-coenzyme M reductase II (second occurrence)	Methanogenesis
29	1.06	Nucleolar protein 56	Ribosome assembly
30	1.04	Proliferating cell nuclear antigen (PCNA)	DNA replication / repair

Table 2: Proteins enriched in the MinD Co-IP of *M. smithii*, ranked by log_2fold change and grouped by functional category

Rank	log_2FC	Protein	Functional category
1	7.80	**MinD (archaeal MinD ATPase; bait)**	Cell division / chromosome partitioning
2	4.22	Alpha-NAC–related protein	Translation / nascent chain association
3	2.72	Putative Zn-finger protein	DNA/RNA binding / regulatory
4	2.45	FKBP-type peptidyl-prolyl cis–trans isomerase	Protein folding / chaperone
5	1.95	DNA topoisomerase I	DNA topology / replication / segregation
6	1.71	dNTP triphosphohydrolase (SAMHD1-like)	Nucleotide metabolism
7	1.69	AAA^+-type ATPase	Protein turnover / chaperone activity
8	1.44	Inositol-3-phosphate synthase	Central metabolism

Table 3: Proteins enriched in the SepF Co-IP of *M. kandleri*, ranked by log_2 fold change and grouped by functional category

A. Proteins significantly enriched in SepF

Rank	log_2FC	Protein	Functional category
1	6.42	**SepF (bait)**	Cell division / divisome
2	4.74	Ribose-5-phosphate isomerase	Central carbon metabolism
3	4.05	YlmC/YmxH family protein	Cell division / divisome-associated
4	2.92	EDR4-like protein (N-terminal)	Stress response / regulation
5	2.77	FUSC-like inner membrane protein	Membrane / transport
6	2.74	**FtsZ**	Cell division / cytoskeleton
7	2.74	N-acetyl-γ-glutamyl-phosphate reductase	Amino acid biosynthesis
8	2.32	Ribosomal protein L10 (60S)	Translation
9	2.04	MTH1895	Unknown
10	1.87	Ribosomal protein eL43	Translation
11	1.85	Iron–sulfur-binding reductase	Energy metabolism
12	1.79	Glutamyl-tRNA(Gln) amidotransferase subunit E	tRNA modification / translation
13	1.78	RecB family endonuclease	DNA replication / repair
14	1.77	Glutamate–cysteine ligase	Amino acid metabolism
15	1.73	Molybdate-binding periplasmic protein	Transport
16	1.68	Phosphoenolpyruvate carboxylase	Central metabolism
17	1.62	Sulerythrin	Oxidative stress response
18	1.52	Phenylalanyl-tRNA synthetase α	Translation
19	1.46	PCNA	DNA replication / genome maintenance
20	1.35	tRNA 4-demethylwyosine synthase	tRNA modification
21	1.35	Diaminopimelate decarboxylase	Amino acid biosynthesis
22	1.33	Ribosomal protein S17	Translation
23	1.31	Methanogenesis marker 13	Methanogenesis
24	1.30	Conserved hypothetical protein	Unknown
25	1.28	Enolase superfamily enzyme	Central metabolism
26	1.26	Ribosomal protein S2	Translation

Rank	log_2FC	Protein	Functional category
27	1.23	dsRBD RNA-binding protein (COG1931)	RNA metabolism
28	1.19	Ribosomal protein L24E	Translation
29	1.14	Imidazoleglycerol-phosphate dehydratase	Amino acid biosynthesis
30	1.12	Peptidase A24B (FlaK)	Protein processing
31	1.10	HybA (Fe-S dehydrogenase subunit)	Energy metabolism
32	1.10	Selenophosphate synthetase	Cofactor / selenium metabolism
33	1.08	Asparagine synthetase	Amino acid biosynthesis
34	1.06	Reverse gyrase (TopG2)	DNA topology / thermophile adaptation
35	1.05	Roadblock/LC7/MglB family protein	Signal transduction
36	1.02	Ribosomal protein uL14	Translation
37	1.02	O-phosphoseryl-tRNA(Sec) transferase	Translation / cofactor biosynthesis
38	1.02	Ribosomal protein S23	Translation

B. Proteins detected only in SepF pulldown

Protein	Functional category
MinD	Cell division / chromosome organization
Replication protein A (RPA70)	DNA replication / repair
DNA polymerase δ (catalytic subunit)	DNA replication
Acetyl-CoA decarboxylase/synthase α	Central metabolism
CRISPR endoribonuclease Csm6	CRISPR / RNA immunity
Archaeosine tRNA-guanine transglycosylase	tRNA modification
NusA	Transcription / RNA metabolism
Adenine-specific DNA methylase	Epigenetic regulation
RNase J2	RNA metabolism
Mechanosensitive channel protein	Membrane / stress response
Methanogenesis markers (2, 16)	Methanogenesis
Hopene cyclase	Membrane lipid metabolism
Multiple DUF proteins	Unknown

References

Bernander, R., & Ettema, T. J. G. (2010). Cell cycle and division in Archaea. *Nature Reviews Microbiology*, 8, 417–428.Adams, D. W., & Errington, J. (2009). Bacterial cell division: assembly, maintenance and disassembly of the Z ring. *Nature Reviews Microbiology*, 7(9), 642–653. https://doi.org/10.1038/nrmicro2198

Eme, L., Spang, A., Lombard, J., Stairs, C. W., & Ettema, T. J. G. (2017). Archaea and the origin of eukaryotes. *Nature Reviews Microbiology*, 15(12), 711–723. https://doi.org/10.1038/nrmicro.2017.133

Makarova, K. S., Yutin, N., Bell, S. D., & Koonin, E. V. (2010). Evolution of diverse cell division and vesicle formation systems in Archaea. *Nature Reviews Microbiology*, 8(10), 731–741. https://doi.org/10.1038/nrmicro2406

van Wolferen, M., Ajon, M., Driessen, A. J. M., & Albers, S.-V. (2022). How archaea divide: division mechanisms and cell cycle regulation. *Nature Reviews Microbiology*, 20(9), 567–582. https://doi.org/10.1038/s41579-022-00711-6

Kandler, O., & König, H. (1998). Cell wall polymers in Archaea (Archaebacteria). *Cellular and Molecular Life Sciences*, 54(4), 305–308. https://doi.org/10.1007/s000180050156

Albers, S.-V., & Meyer, B. H. (2011). The archaeal cell envelope. *Nature Reviews Microbiology*, 9(6), 414–426. https://doi.org/10.1038/nrmicro2576

Meyer, B. H., & Albers, S.-V. (2020). Archaeal cell walls: structures, biosynthesis, and functions. *Nature Reviews Microbiology*, 18(7), 395–407. https://doi.org/10.1038/s41579-020-0360-6

Baumeister, W., & Lembcke, G. (1992). Structural features of archaeal S-layers. *Journal of Bioenergetics and Biomembranes*, 24, 567–575.Zink, I. A., Pfeifer, K., Wimmer, E., Sleytr, U. B., Schuster, B., & Schleper, C. (2019). CRISPR-mediated gene silencing reveals involvement of the archaeal S-layer in cell division and virus infection. *Nature Communications*, 10, 4797. https://doi.org/10.1038/s41467-019-12822-0

König, H., Hartmann, E., & Kandler, O. (2017). Cell wall polymers of Archaea. *Subcellular Biochemistry*, 84, 363–383. https://doi.org/10.1007/978-3-319-46503-6_13

Errington, J. (2015). Bacterial morphogenesis and the enigmatic MreB helix. *Nature Reviews Microbiology*, 13(4), 241–248. https://doi.org/10.1038/nrmicro3398

Vietri, M., Radulovic, M., & Stenmark, H. (2020). The many functions of ESCRT proteins. *Nature Reviews Molecular Cell Biology*, 21(1), 25–42. https://doi.org/10.1038/s41580-019-0177-4

Thanbichler, M. (2010). Synchronization of chromosome dynamics and cell division in bacteria. *Cold Spring Harbor Perspectives in Biology*, 2(11), a000331. https://doi.org/10.1101/cshperspect.a000331

McQuillen, R., & Xiao, J. (2021). Insights into the structure, function, and dynamics of the bacterial cytokinetic FtsZ-ring. *Annual Review of Biophysics*, 50, 309–341. https://doi.org/10.1146/annurev-biophys-101920-094650

Ithurbide, S., Albers, S.-V., Gribaldo, S., & Pende, N. (2022). The cell division machinery of Archaea: a genomic, phylogenetic and cell biological perspective. *FEMS Microbiology Reviews*, 46(2), fuab042. https://doi.org/10.1093/femsre/fuab042

Aylett, C. H. S., & Duggin, I. G. (2017). The tubulin superfamily in Archaea. *Subcellular Biochemistry*, 84, 393–417. https://doi.org/10.1007/978-3-319-46503-6_14

Wagstaff, J. M., & Löwe, J. (2018). Prokaryotic cytoskeletons: protein filaments organizing small cells. *Nature Reviews Microbiology*, 16(4), 187–201. https://doi.org/10.1038/nrmicro.2017.153

Liao, Y., Ithurbide, S., Löwe, J., Duggin, I. G., & Pende, N. (2021). Two FtsZ homologs orchestrate archaeal cell division through distinct functions. *Nature Communications*, 12, 4816. https://doi.org/10.1038/s41467-021-25065-4

Nußbaum, P., Ithurbide, S., Wolferen, M. van, Zhang, H., Duggin, I. G., & Albers, S.-V. (2021). An archaeal SepF-like protein anchors the FtsZ ring at the division site. *Nature Communications*, 12, 657. https://doi.org/10.1038/s41467-021-20933-5

Nußbaum, P., Wolferen, M. van, Zhang, H., Albers, S.-V., & Duggin, I. G. (2023). CdpB proteins form a conserved archaeal divisome module together with SepF. *Nature Microbiology*, 8, 386–398. https://doi.org/10.1038/s41564-022-01287-7

Pende, N., Sogues, A., Bastiaens, P., & Albers, S.-V. (2021). SepF is the FtsZ membrane anchor in methanogenic archaea. *Nature Microbiology*, 6, 1014–1026. https://doi.org/10.1038/s41564-021-00930-7

Duggin, I. G., Aylett, C. H. S., Walsh, J. C., Michie, K. A., Wang, Q., Turnbull, L., … Löwe, J. (2015). CetZ tubulin-like proteins control archaeal cell shape. *Nature*, 519(7543), 362–365. https://doi.org/10.1038/nature13983

Ettema, T. J. G., Lindås, A.-C., & Bernander, R. (2011). An actin-based cytoskeleton in Archaea. *Molecular Microbiology*, 80(4), 1052–1061. https://doi.org/10.1111/j.1365-2958.2011.07635.x

Izoré, T., Kureisaite-Ciziene, D., McLaughlin, S. H., & Löwe, J. (2016). Crenactin forms actin-like double-helical filaments regulated by arcadins. *eLife*, 5, e21600. https://doi.org/10.7554/eLife.21600

Ithurbide, S., Albers, S.-V., Gribaldo, S., & Pende, N. (2022). The cell division machinery of Archaea: A genomic, phylogenetic and cell biological perspective. *FEMS Microbiology Reviews*, 46(2), fuab042. https://doi.org/10.1093/femsre/fuab042

Vecchiarelli, A. G., Li, M., Mizuuchi, M., & Mizuuchi, K. (2014). Differential affinities of MinD and ParA proteins for DNA and membranes coordinate their dynamic localization. *Proceedings of the National Academy of Sciences USA*, 111(32), E3811–E3820. https://doi.org/10.1073/pnas.1408735111

Nußbaum, P., Wolferen, M. van, Zhang, H., Albers, S.-V., & Duggin, I. G. (2020). An oscillating MinD protein determines the cellular positioning of the motility machinery in archaea. *Nature Communications*, 11, 2729. https://doi.org/10.1038/s41467-020-16542-4

Samuel, B. S., & Gordon, J. I. (2006). A humanized gnotobiotic mouse model of host–archaeal–bacterial mutualism. *Proceedings of the National Academy of Sciences USA*, 103(26), 10011–10016. https://doi.org/10.1073/pnas.0602187103

Gaci, N., Borrel, G., Tottey, W., O'Toole, P. W., & Brugère, J.-F. (2014). Archaea and the human gut: New beginning of an old story. *World Journal of Gastroenterology*, 20(43), 16062–16078. https://doi.org/10.3748/wjg.v20.i43.16062

Kurr, M., Huber, R., König, H., Jannasch, H. W., Fricke, H., Trincone, A., … Stetter, K. O. (1991). Methanopyrus kandleri, gen. and sp. nov. represents a novel group of hyperthermophilic methanogens, growing at 110 °C. *Archives of Microbiology*, 156, 239–247. https://doi.org/10.1007/BF00248708

Slesarev, A. I., Mezhevaya, K. V., Makarova, K. S., Polushin, N. N., Shcherbinina, O. V., Shakhova, V. V., … Kozyavkin, S. A. (2002). The complete genome of hyperthermophile Methanopyrus kandleri AV19 and monophyly of archaeal methanogens. *Proceedings of the National Academy of Sciences USA*, 99(7), 4644–4649. https://doi.org/10.1073/pnas.032671499

Pulianmackal, A. J., & Vecchiarelli, A. G. (2024). ParA/MinD family ATPases: Spatial organizers of the prokaryotic cell. *Annual Review of Microbiology*, 78, 195–219. https://doi.org/10.1146/annurev-micro-102722-121256

Parker, A., Marston, A. L., & Wigneshweraraj, S. (2021). Chromosome segregation in bacteria: Emerging roles for ParA ATPases in DNA organization beyond partitioning. *Current Opinion in Microbiology*, 63, 1–8. https://doi.org/10.1016/j.mib.2021.05.003

Duman, R., Ishikawa, S., Celik, I., Strahl, H., Ogasawara, N., & Hamoen, L. W. (2013). Structural and genetic analyses reveal the protein SepF as a new membrane anchor for the Z ring. *Proceedings of the National Academy of Sciences USA*, 110(29), E2601–E2610. https://doi.org/10.1073/pnas.1213560110

Krol, E., van Kessel, S. P., van Bezouwen, L. S., Kumar, N., Boekema, E. J., & Scheffers, D.-J. (2012). Bacillus subtilis SepF binds to the C terminus of FtsZ and promotes bundling of FtsZ protofilaments. *Journal of Bacteriology*, 194(20), 5906–5913. https://doi.org/10.1128/JB.00938-12

Ducret, A., Quardokus, E. M., & Brun, Y. V. (2016). MicrobeJ, a tool for high throughput bacterial cell detection and quantitative analysis. *Nature Microbiology*, 1, 16077. https://doi.org/10.1038/nmicrobiol.2016.77

Webb, M. R. (1992). A continuous spectrophotometric assay for inorganic phosphate and for measuring phosphate release kinetics in biological systems. *Proceedings of the National Academy of Sciences of the United States of America*, 89(11), 4884–4887. https://doi.org/10.1073/pnas.89.11.4884

Hu, Z., & Lutkenhaus, J. (1999). Topological regulation of cell division in *Escherichia coli* involves rapid pole-to-pole oscillation of the division inhibitor MinC under the control of MinD and MinE. *Molecular Microbiology*, 34(1), 82–90. https://doi.org/10.1046/j.1365-2958.1999.01575.x

Szardenings, F., Guymer, D., & Gerdes, K. (2011). ParA ATPases can move and position DNA and protein cargoes. *Current Opinion in Microbiology*, 14(6), 712–718. https://doi.org/10.1016/j.mib.2011.09.003

Vecchiarelli, A. G., Han, Y. W., Tan, X., Mizuuchi, M., Ghirlando, R., Biertümpfel, C., Funnell, B. E., & Mizuuchi, K. (2010). ATP control of dynamic ParA–DNA interactions is essential for plasmid partition. *Molecular Microbiology*, 78, 78–91. https://doi.org/10.1111/j.1365-2958.2010.07306.x

Leonard, T. A., Butler, P. J. G., & Löwe, J. (2005). Structural analysis of the chromosome segregation protein ParA. *EMBO Journal*, 24, 270–282. https://doi.org/10.1038/sj.emboj.7600521

Wagstaff, J. M., & Löwe, J. (2018). Prokaryotic cytoskeletons: protein filaments organizing small cells. *Nature Reviews Microbiology*, 16, 187–201. https://doi.org/10.1038/nrmicro.2017.153

Aylett, C. H. S., & Duggin, I. G. (2017). The tubulin superfamily in Archaea. *Subcellular Biochemistry*, 84, 393–417. https://doi.org/10.1007/978-3-319-46503-6_14

Mishra, A., Choudhary, A., & Tiwari, S. (2021). Xenusia: a machine learning-based approach for DNA-binding protein prediction. *Briefings in Bioinformatics*, 22, bbab178. https://doi.org/10.1093/bib/bbab178

Lazar, C., et al. (2016). Accounting for the multiple natures of missing values in label-free quantitative proteomics data. *Bioinformatics*, 32, 1416–1423. https://doi.org/10.1093/bioinformatics/btw041

Vieille, C., & Zeikus, G. J. (2001). Hyperthermophilic enzymes: sources, uses, and molecular mechanisms for thermostability. *Microbiology and Molecular Biology Reviews, 65*(1), 1–43. https://doi.org/10.1128/MMBR.65.1.1-43.2001

Schumacher, M. A. (2012). Bacterial plasmid partition machinery: a minimalist approach to survival. *Current Opinion in Structural Biology, 22*(1), 72–79. https://doi.org/10.1016/j.sbi.2011.11.001

Mohl, D. A., & Gober, J. W. (1997). Cell cycle–dependent polar localization of chromosome partitioning proteins in *Caulobacter crescentus*. *Cell, 88*(5), 675–684. https://doi.org/10.1016/S0092-8674(00)81910-8

Takemata, N., & Bell, S. D. (2021). Emerging views of genome organization in archaea. *Journal of Molecular Biology*, *433*(14), 166932. https://doi.org/10.1016/j.jmb.2021.166932

Kelman, Z., & White, M. F. (2005). Archaeal DNA replication and repair. *Current Opinion in Microbiology, 8*(6), 669–676. https://doi.org/10.1016/j.mib.2005.10.001

Grogan, D. W. (2015). Understanding DNA repair in hyperthermophilic archaea. *Current Opinion in Microbiology, 25*, 59–65. https://doi.org/10.1016/j.mib.2015.04.003

Lichtman, J. W., & Conchello, J.-A. (2005). Fluorescence microscopy. *Nature Methods, 2*(12), 910–919. https://doi.org/10.1038/nmeth817

Cobbe, N., & Heck, M. M. S. (2004). SMC proteins in the maintenance of genome stability. *Trends in Biochemical Sciences, 29*, 406–415. https://doi.org/10.1016/j.tibs.2004.06.005

Fink, M., et al. (2021). Genetic tools for Methanobacterium thermoautotrophicum. *Frontiers in Microbiology, 12*, 682039. https://doi.org/10.3389/fmicb.2021.682039

Hirano, T. (2016). Condensin-based chromosome organization. *Cold Spring Harbor Perspectives in Biology, 8*, a018994. https://doi.org/10.1101/cshperspect.a018994

Robinson, N. P., et al. (2007). Identification of two origins of replication in the single chromosome of Sulfolobus solfataricus. *Cell, 130*, 879–890. https://doi.org/10.1016/j.cell.2007.07.047

Schumacher, M. A., et al. (2015). Structures of archaeal chromosome segregation proteins SegA and SegB. *eLife, 4*, e09623. https://doi.org/10.7554/eLife.09623

Thauer, R. K., Kaster, A.-K., Seedorf, H., Buckel, W., & Hedderich, R. (2008). Methanogenic archaea: ecologically relevant differences in energy conservation. *Nature Reviews Microbiology, 6*, 579–591.https://doi.org/10.1038/nrmicro1931